



The impact of evolving mineral–water–gas interfacial areas on mineral–fluid reaction rates in unsaturated porous media



Anna L. Harrison ^{*,1}, Gregory M. Dipple, Ian M. Power, K. Ulrich Mayer

Mineral Deposit Research Unit, Department of Earth, Ocean and Atmospheric Sciences, The University of British Columbia, 2207 Main Mall, Vancouver, British Columbia V6T 1Z4, Canada

ARTICLE INFO

Article history:

Received 3 September 2015

Received in revised form 2 December 2015

Accepted 14 December 2015

Available online 15 December 2015

Keywords:

Unsaturated zone
Mineral carbonation
Water-limited reaction
Surface passivation
Reactive surface area
Stable carbon isotopes
CO₂ sequestration

ABSTRACT

The distribution and evolution of mineral–water–gas interfacial areas exert a fundamental yet poorly documented control on mineral–fluid reactions in the unsaturated zone. Here, we explore the impact of changing mineral reactive surface area, water content, and gas distribution on the reaction of brucite [Mg(OH)₂] with CO₂ gas to form hydrated Mg-carbonate minerals in partially water saturated meter-scale column experiments. Brucite surface area, which is inferred to exert a direct control on mineral dissolution rates, demonstrates a complex evolution including roughening, fracturing and passivation that is inconsistent with conventional models of geometric evolution. Mineral–fluid reaction in the interior of single brucite grains maintains surface area at near-constant values despite the decreasing volumetric brucite content, until solid carbonate precipitates passivate brucite surfaces. The evolution of reactive surface area during passivation also does not follow simple geometric processes. A porous amorphous carbonate phase permits ready access to brucite surfaces for reaction until recrystallization of the amorphous carbonate into bladed, low-porosity nesquehonite [MgCO₃·3H₂O] abruptly quenches reaction. The varied water content of the experiments illustrates that the extent of mineral–gas reaction is limited by the abundance of water available to facilitate precipitation of hydrated carbonate minerals. Conversely, at high bulk water saturation, the development of preferential gas flow paths limited the exposure of reactive minerals to CO₂ and reduced the overall extent of reaction. Thus, bulk mineral–fluid reaction rates were reduced at both high and low bulk water contents.

© 2015 Elsevier B.V. All rights reserved.

1. Introduction

Mineral weathering in the unsaturated zone, where the pores are only partially water-filled, is an important control on nutrient availability, contaminant transport, and the carbon cycle (e.g., Maher et al., 2009; Manning, 2008; McKinley et al., 2006). The rate at which these reactions occur depends on the available reactive surface area in contact with a reactive fluid (e.g., Brantley and Mellot, 2000; Helgeson et al., 1984), a variable that is dependent on both the physical and chemical properties of the mineral, and environmental conditions such as water saturation (White and Brantley, 2003). In the unsaturated zone, quantification of reactive surface area is complicated by several factors, including heterogeneous water distribution and secondary phase precipitation, which can dictate solution chemistry and passivate reactive surfaces (Brantley, 2008; Maher et al., 2009; Pačes, 1983; Scislawski and Zuddas, 2010; White and Brantley, 2003). Moreover, the reactive surface area may change over time due to consumption of the reactive

phase, preferential dissolution of defects and highly reactive sites, alteration of surface morphology, and formation of surface coatings (Daval et al., 2009; Harrison et al., 2015; Helgeson et al., 1984; Maher et al., 2006; Petrovich, 1981; Scislawski and Zuddas, 2010; White and Brantley, 2003). Environmental factors are also highly variable over time in natural systems; water saturation in the shallow subsurface is modified in response to short-term weather events and longer-term climate change that may alter the exposure of mineral surfaces to water, and the development of preferential flow paths may decrease exposure to reactants. At low water contents the extent of reaction of mineral phases may be limited due to a lack of water available to facilitate dissolution–precipitation reactions and incorporate into secondary hydrous minerals (Assima et al., 2013a; Felmy et al., 2012; Harrison et al., 2015; Loring et al., 2011; Miller et al., 2013; Schaef et al., 2013; Bea et al., 2012; Thompson et al., 2013). Here, we aim to assess the evolution of effective (i.e., available) reactive surface area during coupled brucite [Mg(OH)₂] dissolution–carbonate precipitation under variably water saturated conditions using meter-scale column reactors. As a follow-up to our previous, smaller scale column experiments that investigated brucite carbonation (Harrison et al., 2015), the much larger experimental scale in the present study provides valuable new insights into processes that operate at a greater length scale, and is an important step towards improved extrapolation of experimental results to the field

* Corresponding author.

E-mail addresses: anna.harrison@stanford.edu (A.L. Harrison), gdipple@eos.ubc.ca (G.M. Dipple), ipower@eos.ubc.ca (I.M. Power), umayer@eos.ubc.ca (K.U. Mayer).

¹ Current address: Department of Geological Sciences, Stanford University, 450 Serra Mall, Stanford, CA 94305, United States.

scale. Moreover, the longer flow-path accessed a more dynamic range in experimental variables (e.g., water content) within a single experiment, and allowed for improved spatial and temporal resolution of reaction progress due to the installation of sensors and sampling ports, which were not available in the smaller scale apparatus of Harrison et al. (2015).

The reaction of brucite and other alkaline earth metal-bearing hydroxide and silicate minerals with CO₂ to form carbonate minerals is known as mineral carbonation (e.g., Lackner et al., 1995). Mineral carbonation reactions are ideal for studying reactive surface area evolution because of the coupled nature of the reaction and relatively high extent of reaction that can be achieved on experimental time scales (Harrison et al., 2015). As a natural weathering reaction, mineral carbonation is an important part of the global carbon cycle and regulates atmospheric CO₂ concentrations over geologic time (Berner et al., 1983). These reactions may also be harnessed as engineered CO₂ sequestration strategies, for instance by injection of CO₂-rich gases or fluids in the subsurface or alkaline waste stockpiles (Bobicki et al., 2012; Gislason et al., 2010; Kelemen and Matter, 2008; McGrail et al., 2006; Power et al., 2013b), or direct air capture via enhanced weathering of pulverized rock or wastes (Assima et al., 2012, 2013a, 2013b; Pronost et al., 2011; Renforth et al., 2009, 2011; Schuiling and de Boer, 2010; Washbourne et al., 2012; Wilson et al., 2006, 2009, 2014). Brucite carbonation is of specific interest for CO₂ sequestration (e.g., Fricker and Park, 2013; Hövelmann et al., 2012b; Li et al., 2014; Nduagu et al., 2013; Zhao et al., 2010), particularly as a component of ultramafic mine wastes that can be exploited for its high reactivity (Assima et al., 2012, 2013a,b; Bea et al., 2012; Beinlich and Austrheim, 2012; Harrison et al., 2013a, 2013b, 2015; Pronost et al., 2011; Wilson et al., 2014). Reactions in these environments tend to occur under variably water saturated conditions (e.g., Bea et al., 2012; Wilson et al., 2014). The study of brucite carbonation therefore allows assessment of fundamental controls on reactivity during coupled dissolution–precipitation reactions in the unsaturated zone, with important implications for offsetting anthropogenic greenhouse gas emissions responsible for global climate change.

The objectives of this study were to 1) investigate the evolution of reactive surface area during coupled brucite dissolution–carbonate mineral precipitation, 2) evaluate the influence of water saturation on extent of reaction in variably water-saturated conditions, and 3) elucidate key processes controlling the rate and extent of CO₂ sequestration that may be achieved by engineered CO₂ sequestration strategies in the shallow subsurface.

2. Methods

2.1. Experimental setup

Column experiments were used to investigate the evolution of reactive surface area during dissolution–precipitation reactions in the unsaturated zone (Fig. 1). In order to examine the impacts of water saturation on rates, extent, and distribution of reaction, experiments with heterogeneous water content and different initial water saturation profiles were performed. A total of three experiments were conducted in 25 cm diameter × 90 cm tall acrylic columns that contained 10 wt.% pulverized brucite ore and 90 wt.% quartz sand (Fig. 1). Of these, two were duplicates with 35% bulk water saturation and one had 60% bulk water saturation. The duplicate experiments are henceforth referred to as “35% 1 and 2.” The 60% saturated column provided a greater total water volume and allowed a greater portion of the column to be at or near 100% pore water saturation in the otherwise identical columns. The brucite ore was pulverized to between 250 and 500 μm in diameter (mass weighted median ≈ 188 μm as estimated based on sieving; refer to the Supplementary Material (SM) for details; SM Fig. S1). The quartz sand was a product of Lane Mountain Materials (“LM 50”) that had been sieved to between 53 and 425 μm.

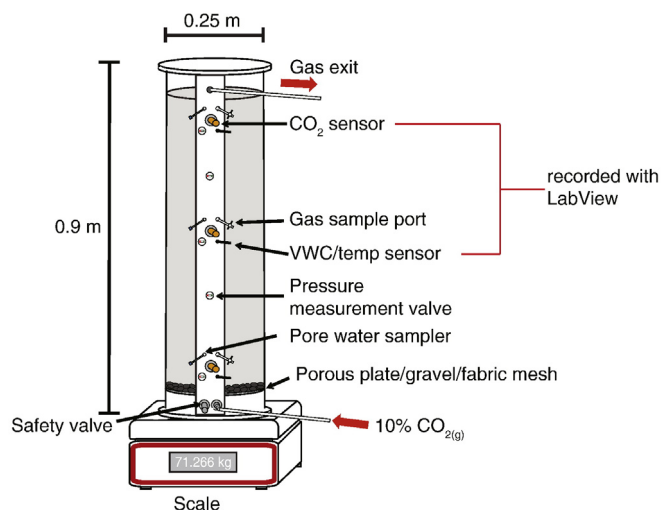


Fig. 1. Schematic of experimental setup.

The initial major oxide composition of the brucite ore and quartz sand was determined using X-ray fluorescence spectroscopy (XRF; refer to SM). XRF measurements indicated that the oxides present in the brucite ore at $\geq 1.00\% \pm 1\sigma$ abundance were: MgO ($60.16 \pm 0.43\%$), SiO₂ ($2.71 \pm 0.04\%$), and CaO ($2.04 \pm 0.03\%$), with $34.29 \pm 0.43\%$ loss on ignition. The quartz sand was $99.10 \pm 0.28\%$ SiO₂, with the remainder consisting primarily of Al₂O₃. Rietveld refinement of X-ray diffraction (XRD) data from analysis of the quartz sand indicated it was nearly 100% pure with trace mica (biotite or muscovite at ≤ 1.0 wt.% abundance). Analysis of triplicate samples of the brucite ore indicated it contained 78.8 ± 3.8 wt.% brucite, 5.5 ± 0.4 wt.% dolomite, 1.9 ± 0.3 wt.% magnesite, 7.4 ± 1.0 wt.% hydromagnesite, and <0.5 wt.% lizardite and pyroaurite. The remainder was amorphous content. The surface area of the brucite ore was determined on duplicate samples using BET with N₂ adsorption, with the average equal to $2.4 \text{ m}^2 \text{ g}^{-1}$.

Mixtures of 10 wt.% brucite ore and 90 wt.% quartz were prepared by mechanically mixing 4.5 kg of brucite ore, and 40.5 kg of quartz sand (total mass = 45.0 kg). The mixtures were wetted with approximately half of the total desired water volume prior to being loaded into the column. The added solution had 0.1 M MgCl₂ and $<1.7 \times 10^{-4}$ M dissolved inorganic carbon (DIC). The partially wetted mixtures were loaded into the columns and compacted by manual compression, with the final height of the porous medium equal to 72 cm in all experiments. After loading, additional MgCl₂ solution was applied to the top of the column in order to reach the desired saturation using a watering can to minimize surface disturbance. The solution was allowed to infiltrate under the force of gravity. The porosity was approximately 0.52–0.54 for all columns, as estimated based on the bulk density of the solids and the height of the porous medium, for a total porous medium volume of 35.4 L.

The columns were continuously flushed with N₂ gas at $\sim 220 \pm 25 \text{ mL min}^{-1}$ overnight to remove laboratory air from the pore space prior to initiating the supply of CO₂, and to allow time for the water distribution to equilibrate. The CO₂ supply was begun without interrupting the flow of N₂, such that the total gas flow rate was $\sim 250 \pm 25 \text{ mL min}^{-1}$ and the supplied gas was 10 vol.% CO₂. The gas entered through a hose barb into the base of the column, and through a porous ceramic plate overlain by a 2 cm thick gravel layer and a sheet of fabric mesh to promote homogeneous distribution of the gas into the brucite/quartz medium (Fig. 1). The top of the column was sealed with a gas-tight acrylic lid, and the gas effluent exited through an outlet at the top of the column (Fig. 1). The flow rate of the gas effluent was measured at least twice a day using a Cole-Parmer® direct reading flow meter.

Sensors and sampling ports were installed at three points along the column length at (1) the base (5 cm above the gravel), (2) the middle (35.5 cm above the gravel), and (3) the top (65.5 cm above the gravel). Each port consisted of a Vaisala® GMT221 CO₂ concentration sensor (measurement error ± 0.5% CO₂), a Decagon 5TM soil moisture and temperature probe (measurement error ± 1 °C, ± 2% volumetric water content), tubing from which to extract gas samples, a SoilMoisture micro pore water sampler, and a Mininert® valve to allow pressure measurements (Fig. 1). A Mininert® valve was also located between each sampling port, for a total of five measurement points. The data from the CO₂ and soil moisture and temperature probes were recorded every 5 or 10 min using National Instruments® LabVIEW™ 8.6 software (National Instruments, 2008).

Water and gas samples were removed every 2–8 h for at least the first 24 h, after which the sampling interval was lowered to once a day or once every two days as the reaction slowed. Pressure was measured manually before each sampling time using a Dwyer® Mark II plastic manometer (measurement error ± 23.2 Pa). Gas samples were collected for measurement of the stable carbon isotopic composition ($\delta^{13}\text{C}$) of the CO₂ using a Los Gatos Research instrument for laser spectroscopy (Barker et al., 2011). All $\delta^{13}\text{C}$ values are reported in δ -notation relative to Vienna Pee Dee Belemnite (VPDB) in units of per mil (‰). Water samples were collected for determination of pH, Mg and DIC concentration, and the $\delta^{13}\text{C}_{\text{DIC}}$. The solution pH was measured immediately after sampling. DIC and $\delta^{13}\text{C}_{\text{DIC}}$ data were unavailable from 35% 1 due to the formation of precipitates while in storage.

The experiments were conducted until they reached an approximate steady-state, with little to no measurable CO₂ reacting along most of the column length, as judged by the recovery of the CO₂ breakthrough curves to approximately the composition of the supplied gas. Hence, the duration of the experiments varied between 430 and 504 h. Following completion of each experiment the entirety of the solid material was removed in 10 cm intervals for analysis of the mineralogical composition, the total solid phase CO₂ content, and the $\delta^{13}\text{C}$ of the carbonate minerals. The major oxide composition and volatile content of the solids was also determined for 35% 1 and the 60% saturated experiment using XRF spectroscopy. For at least three of the depth intervals in each column, triplicate discrete samples were taken to assess heterogeneity in reaction extent and mineralogy. The remaining intervals were mechanically homogenized and an aliquot of the bulk material was removed for analysis. Experimental products were examined using scanning electron microscopy (SEM). Water saturation with depth was estimated by gravimetric measurement of aliquots of bulk porous medium before and after drying at 70 °C. Total water content at the end of the experiments was estimated for 35% 2 and the 60% saturated column experiments by collection, drying, and weighing of all reaction products upon completion of the experiments.

2.2. Assessment of the rate and extent of carbonation

The extent of reaction was estimated using several lines of evidence, including (1) the total carbon content in the solid phase (%CO₂), (2) the mass gain of the columns during the course of the experiment, (3) the abundance of mineral phases, and (4) the reduction of CO₂ content in the gas phase. The %CO₂ and mineral abundance data provided information as to heterogeneity in reaction extent and mineralogical distribution, whereas the gravimetric and gas phase CO₂ measurements were used to estimate the total CO₂ sequestered, and the latter to determine the rate of carbonation. The total carbon content for all experiments is expressed as %CO₂ by mass and was measured using coulometry (refer to SM). The initial brucite/quartz mixtures had an average of 0.65% CO₂ that was contained in dolomite, hydromagnesite, and magnesite present in the initial brucite ore. This initial mass of CO₂ was subtracted from CO₂ content values measured for reacted samples to determine the mass of CO₂ gained. This was justified by the presence

of approximately the same mass of dolomite in the reaction products as in the initial material as determined using XRD, although the data were insufficient to resolve changes in hydromagnesite and magnesite abundances. In order to estimate the CO₂ gain gravimetrically, the columns were placed on a scale with ± 20 g accuracy and their mass was recorded three to four times a day. The abundance of secondary carbonate phases and reduction in brucite content was determined using Rietveld refinement of XRD data. A known mass of highly crystalline fluorite [CaF₂] was added to solid aliquots to assess whether CO₂ was also stored in X-ray amorphous carbonate phases (e.g., Gualtieri, 2000). Finally, because the flux of CO₂ into the column was known, the mass of CO₂ sequestered and carbonation rate were also determined based on the reduction in this flux along the column length as measured using the CO₂ concentration sensors (refer to SM). The CO₂ breakthrough curves measured with the sensors are expressed as 'C/C₀', the ratio of the CO₂ concentration in the gas effluent at a given time to the concentration of CO₂ in the supplied gas. For further detail regarding the experimental setup and analytical techniques, refer to the Supplementary Material (SM).

2.3. Geochemical and reactive transport modeling

The variation in mineral saturation indices with reaction progress was calculated based on the measured aqueous chemistry data using PHREEQC V.3 (Parkhurst and Appelo, 2013) with the Pitzer database and mineral solubility data from the Minteq database. The saturation index is defined as the logarithm of the ratio of the ion activity product to the equilibrium constant. Reaction progress under the experimental conditions was simulated using the multicomponent reactive transport code MIN3P-DUSTY (Mayer et al., 2002; Molins and Mayer, 2007), which comprises a suite of chemical reactions including mineral dissolution–precipitation, and can model flow and transport in both the gaseous and aqueous phases. Gas transport was modeled as an advective–diffusive process according to Darcy's law and the Dusty Gas model (Mason and Malinauskas, 1983; Molins and Mayer, 2007). For a complete description of the constitutive equations refer to Mayer et al. (2002) and Molins and Mayer (2007). Brucite dissolution kinetics were modeled using a HCO₃⁻ concentration-dependent kinetic dissolution rate law based on data from Pokrovsky et al. (2005) and Pokrovsky and Schott (2004) (Eqs. (1) and (2)):

$$r_{brc} = k_{eff}^0 [\text{HCO}_3^-]^{0.56} (1 - \Omega^2) \quad (1)$$

$$k_{eff}^0 = k^0 SA \quad (2)$$

where r_{brc} is the brucite dissolution rate (mol s⁻¹), k_{eff}^0 is the effective rate constant, k^0 is the initial reaction rate constant equal to 10^{-6.13} L s⁻¹ m⁻², SA is the brucite surface area (m²), and Ω is the saturation ratio. Saturation ratio is defined as the ratio of the ion activity product to the equilibrium constant.

The identities and rates of formation of secondary phases were selected based on experimental results. The two precipitates were an X-ray amorphous phase and nesquehonite [MgCO₃·3H₂O], the former having stoichiometry and solubility similar to artinite (refer to the Results section). Precipitation of artinite [Mg₂CO₃(OH)₂·3H₂O] was modeled effectively as an equilibrium process, but nesquehonite precipitation was slowed such that precipitation occurred at supersaturated conditions, in accordance with experimental data. Porosity was set to a representative value of 0.52 for all simulations, and soil hydraulic function parameters were estimated based on results of Tempe cell tests of the solid materials (e.g., Fredlund and Rahardjo, 1993) and measured water saturation profiles. For a complete list of transport parameters used in the simulations and results of Tempe cell tests, refer to the Supplementary Material (SM Fig. S2; SM Tables S2 and S3).

3. Results

3.1. Rate and extent of carbonation

The CO₂ concentration in the gas phase (CO₂ breakthrough curves) varied significantly with depth in all experiments (Fig. 2). Similar trends were documented in the duplicate experiments, although a slightly higher CO₂ concentration was measured by the middle sensor in 35% 2 during the first ~100 h (Fig. 2), which may indicate the presence of preferential flow paths. Four distinct carbonation stages were evident in the breakthrough curves (Fig. 2), as is in agreement with observations of brucite carbonation in smaller scale experiments (Harrison et al., 2015). Stage 1 represents rapid reaction of brucite powder coating the brucite grains that was an artifact of the pulverization process. Previous experimental results revealed that this powder does not consume a significant mass of CO₂, or affect reaction rates after stage 1 (Harrison et al., 2015). Stage 2 is the reaction of the bulk of the brucite. Stage 3 comprises a rapid decline in reaction rate due to loss of reactive brucite. Finally, stage 4 is when the reaction rate becomes negligible because any remaining brucite is effectively inaccessible for reaction. However, during stage 4 the CO₂ concentration did not quite return to its inflow value ($C/C_0 < 1$), implying that carbonation reactions were still slowly proceeding. Diurnal fluctuations in $p\text{CO}_2$ (<0.4%) measured at the top of the columns were coincident with temperature variations in the laboratory (SM Fig. S3a). The experimental apparatus was not insulated, thus the pore water temperature experienced fluctuations in response to variations in the laboratory air temperature (SM Fig. S3a).

Substantial differences were evident between the breakthrough curves of the 35% and 60% saturated columns (Fig. 2). In the 60% saturated column, the CO₂ concentration measured at the middle sensor was virtually identical to that measured at the base, indicative of transport of CO₂ along preferential flow paths. Similarly, CO₂ reached the top of the column at measurable concentrations earlier in the 60% saturated column, at ~16 h compared to ~80 h in the 35% saturated columns.

The CO₂ breakthrough at the top of the columns was used to calculate the bulk rate of carbonation over time. Carbonation rates in Fig. 3 are normalized to the CO₂ supply rate for ease of comparison, as slight differences (10% relative) in gas flow rate were documented between experiments. These calculations revealed that the rate of carbonation was comparable between the duplicate 35% saturated columns, and these rates exceeded that in the 60% saturated column for the majority of the experimental duration (Fig. 3).

The extent of carbonation in each experiment as calculated using the reduction of CO₂ content in the gas phase and the total mass gain during the course of the experiments agreed fairly well (Fig. 3), except for 35% 1, for which the gravimetric estimate was ~17% lower than

indicated by the gas phase measurements. Gravimetric measurements indicated that 528 g, 566 g, and 476 g were gained in 35% 1 and 2, and the 60% saturated experiments, respectively. Changes in gas phase CO₂ concentrations with time indicated that 635 g, 587 g, and 469 g of CO₂ were gained in 35% 1 and 2, and 60% saturated experiments, respectively. As the gravimetric measurements were not corrected for evaporation due to difficulty controlling and measuring evaporation rates between experiments, these values represent the minimum mass of CO₂ gained. This could account for the discrepancy between the two types of measurements, and would imply that the evaporation rate was highest for 35% 1. Importantly, both datasets indicated that the least amount of CO₂ was sequestered in the 60% saturated column. In all cases, the amount of CO₂ sequestered was significantly less than the theoretical sequestration capacity of ~2676 g CO₂ assuming complete conversion of brucite to nesquehonite. Only 24%, 22%, and 18% of the theoretical CO₂ sequestration capacity was achieved.

3.2. Characterization of precipitates

3.2.1. Composition and distribution of precipitates

In all experiments, brucite was replaced by nesquehonite and an X-ray amorphous Mg-carbonate phase (Fig. 4; SM Fig. S4). A minor amount of lansfordite [MgCO₃·5H₂O] was also documented in 35% 1 (Fig. 4C). Only total amorphous content can be calculated using Rietveld refinement, therefore quantified abundances of the X-ray amorphous Mg-carbonate include any amorphous content in other phases. Thus, the XRD quantified abundance was not used to calculate the mass of this phase, but nevertheless allowed assessment of the general trends in abundance. Nesquehonite was not resolved above ~35 cm depth, but %CO₂ measurements indicated that CO₂ was still sequestered (Fig. 4C and D). This confirms that the X-ray amorphous phase was also a carbonate, in agreement with energy dispersive spectroscopy results (SM Fig. S7) and previous experiments (Harrison et al., 2015). The abundance of both Mg-carbonates tended to decrease with distance along the flow path in all experiments, although significant heterogeneity in the extent of carbonate precipitation was documented in triplicate samples from the same depth intervals (Fig. 4B and C). The greatest extent of heterogeneity for both the carbonate minerals and total %CO₂ was documented in the 60% saturated column, and towards the bases of all columns where the water saturation was generally highest (Fig. 4). Due to the high degree of heterogeneity in the extent of carbonation, these data were not used to calculate the total mass of CO₂ sequestered. Nowhere was brucite completely consumed, but the abundance typically increased along the flow path in parallel to the decreased %CO₂ sequestered (Fig. 4A). An orange coloration in

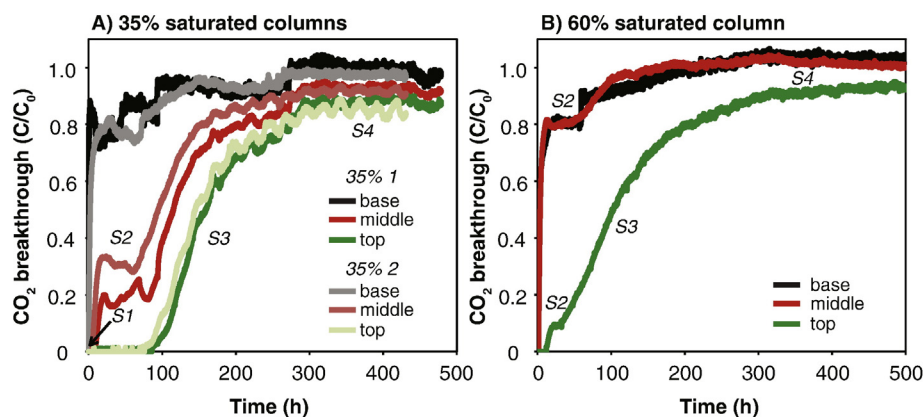


Fig. 2. CO₂ breakthrough curves at three positions along the flow path plotted as C/C_0 (ratio of the measured CO₂ concentration at the measurement port to the CO₂ concentration in the supplied gas) versus time. Black, red, and green lines show the CO₂ breakthrough curves measured at the base, middle, and top of the 35% saturated columns (A) and the 60% saturated column (B). "SX" labels denote reaction stages 1 through 4.

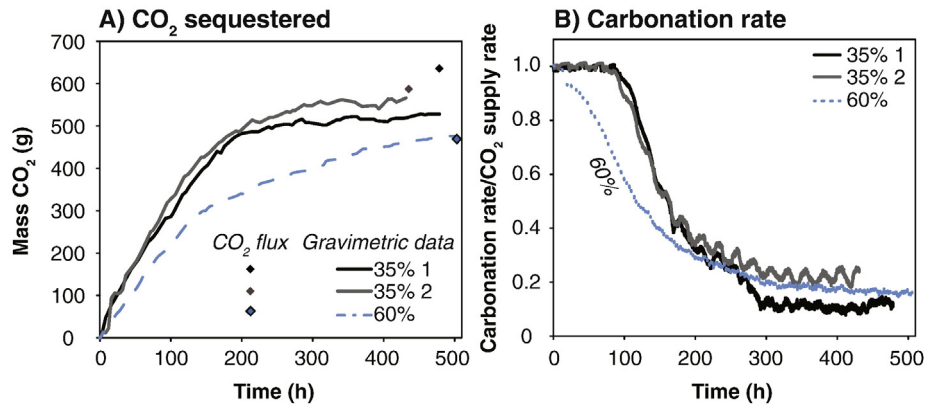


Fig. 3. Mass of CO₂ sequestered versus time (A) and instantaneous carbonation rate versus time (B). Black, gray, and blue lines represent gravimetric measurements of 35% 1 and 2, and the 60% saturated columns, respectively. Diamonds in (A) show cumulative CO₂ mass sequestered based on CO₂ flux analysis. (For interpretation of the references to color in this figure legend, the reader is referred to the web version of this article.)

reaction products was found to correlate with a greater extent of carbonation (SM Fig. S5).

The stoichiometry of the X-ray amorphous phase was estimated by mass balance with XRF, XRD, and %CO₂ data for samples from 35% 1 and the 60% saturated column (refer to the SM). Only samples without measurable nesquehonite were used for the calculations, as the stoichiometry of precipitated nesquehonite may not be ideal, thereby introducing additional error into the stoichiometry calculation. The average Mg:C and H₂O:Mg molar ratios calculated for the X-ray amorphous phase in 35% 1 were 2.2 and 1.4, respectively. The average Mg:C and H₂O:Mg ratios calculated for this phase in the 60% saturated column were 1.9 and 1.6, respectively. The estimated chemical formula of the X-ray amorphous phase is thus postulated to be Mg₂CO₃(OH)₂·~2H₂O. This is similar to the composition of the known hydrated Mg-carbonate phase, artinite [Mg₂CO₃(OH)₂·3H₂O], and confirms the stoichiometry calculated from our smaller scale experiments

using a more robust dataset (Harrison et al., 2015). We refer to this precipitate as pseudo-artinite.

3.2.2. Textural characterization of precipitates

Brucite ore was coated with a fine brucite powder that was an artifact of the crushing process (SM Fig. S6). This fine powder was absent in samples examined upon completion of the experiments. Precipitates of two morphologies were observed in all columns; long, narrow crystals with morphology typical of nesquehonite (e.g., Assima et al., 2013a; Harrison et al., 2015; Power et al., 2007; Schaefer et al., 2011), and a fine, flakey material coating surfaces (Fig. 5A). Energy dispersive spectroscopy confirmed that both of these phases consisted of Mg, C, and O (SM Fig. S7). The morphology of the flakey material is similar to that observed for an X-ray amorphous carbonate of comparable stoichiometry precipitated under similar experimental conditions (Harrison et al., 2015). The flakey material is abundant in samples

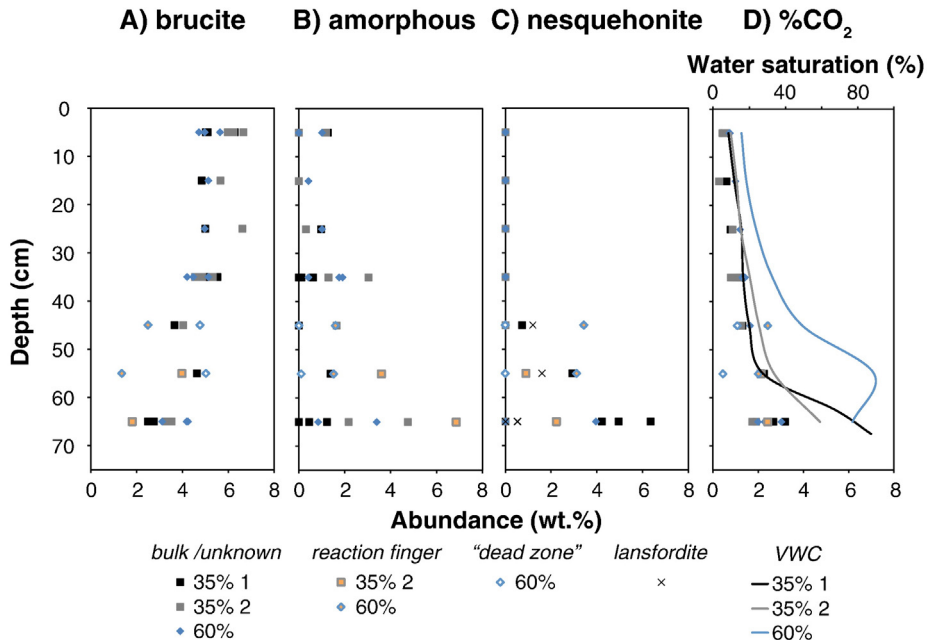


Fig. 4. Mineral and solid phase CO₂ abundance profiles. A) Brucite abundance versus depth. B) Amorphous content versus depth. C) Nesquehonite abundance versus depth from all columns, and lansfordite abundance versus depth in 35% 1. D) Total solid phase CO₂ content in the experimental products that is contained in secondary carbonate phases and final water saturation versus depth. Black and gray squares represent 35% 1 and 2, respectively. Blue diamonds represent the 60% saturated column experiment. Black, gray, and blue lines represent the water saturation of 35% 1 and 2, and the 60% saturated experiment, respectively. Black 'Xs' in (C) represent lansfordite abundance in 35% 1; lansfordite was not detected in the other experiments. Orange-filled symbols represent samples taken from reaction fingers, and white-filled symbols represent samples taken from "dead-zones" outside fingers. All others represent bulk samples or samples for which it was not possible to ascertain visually whether they were part of a reaction finger.

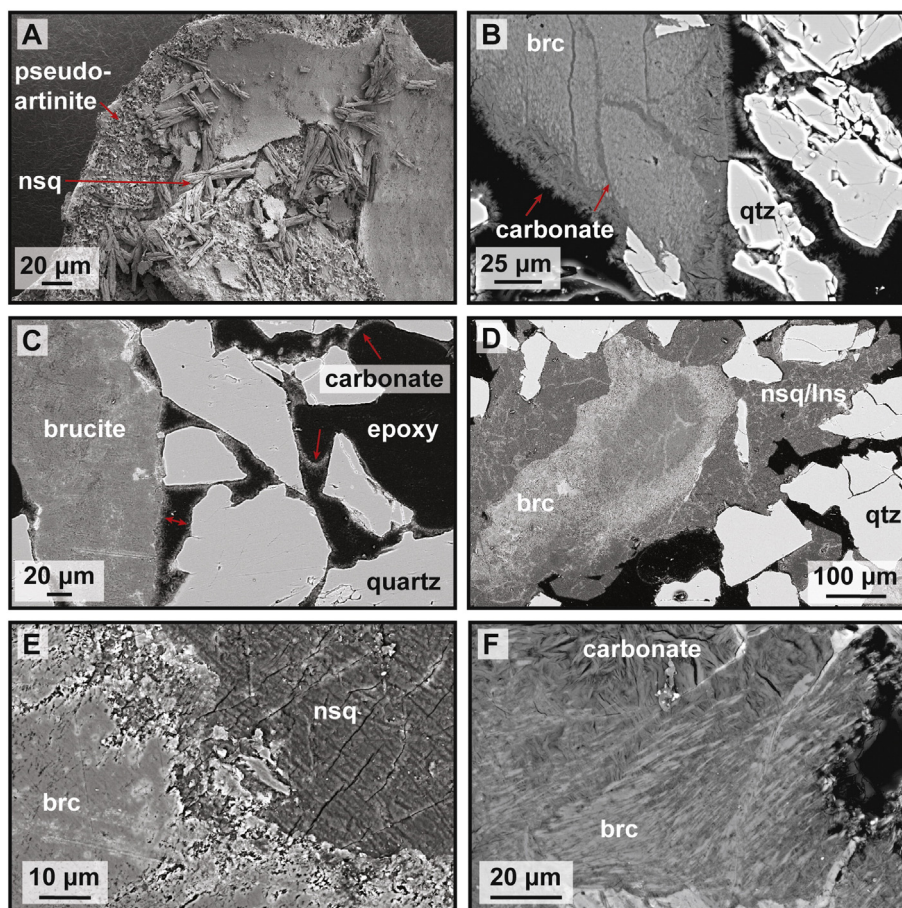


Fig. 5. Representative scanning electron micrographs of experimental products. A) Secondary electron micrograph showing flakey pseudo-artinite with nesquehonite (nsq) needles on top from 30 to 40 cm depth in the 60% saturated column (~30% saturation). Images B through F are backscattered electron micrographs. B) A brucite grain with carbonate coating and channels infilled with carbonate that extend into the interior of the grain from 60 to 70 cm depth in the 60% saturated column (>80% saturation). C) Flakey carbonate coating (~5 μm thick; red arrows) surrounding brucite and quartz particles and lining the location of the gas–water interface (right half of micrograph) in an area with locally low water content (~10% saturation) from 20 to 30 cm depth in 35% 1. D) Thick carbonate rind (>100 μm) extending from a partially carbonated brucite particle in an area with locally high water content (~90% saturation) from 65 to 70 cm depth in 35% 1. E) The edge of a brucite grain with pieces “lifted” from the surface and encrusted in precipitated carbonate from 65 to 70 cm depth in 35% 1 (~90% saturation). F) Thin remnants of brucite interspersed with carbonate precipitates in an extensively carbonated area from 60 to 70 cm depth in the 60% saturated column (>80% saturation). Lighter gray areas are brucite, darker gray is secondary carbonate, and black is epoxy. (For interpretation of the references to color in this figure legend, the reader is referred to the web version of this article.)

known to be rich in pseudo-artinite, to which we attribute this morphology. Nesquehonite needles were observed to rim pseudo-artinite (Fig. 5A). The distribution of these two reaction products changed significantly with distance along the flow path. Near the base of the column, where water contents were high, large crystals of nesquehonite or lansfordite were observed to form 10–100s of μm thick rinds surrounding partially reacted brucite grains (Fig. 5D and E). Precipitates were also documented to form pervasive cements that extended across several pore bodies even where brucite grains were lacking (Fig. 5D). Brucite surfaces were rough, with pieces lifted off the surface in some cases and thin pieces of brucite isolated between carbonate precipitates (Fig. 5E and F). Cracks filled with carbonate precipitates were also observed to extend well within some brucite grains (Fig. 5B). Further along the flow path, in the relatively dry upper portion of the columns, precipitates instead formed as thin (~5 μm), flakey coatings surrounding both brucite and quartz grains (Fig. 5C). Carbonate precipitates in thin section mimicked the curvature of the water meniscus at the gas–water interface, as approximated by visible curvatures in the epoxy–mineral interface (Fig. 5C). The local water saturation can therefore be estimated based on the location of these interfaces. At low water saturation, carbonate precipitates are restricted to narrow regions where water films were present (Fig. 5C). The flakey carbonates were also observed to line the “gas–water interfaces,” but were typically not present

in the middle of larger pore bodies (Fig. 5C), in contrast to the wetter areas of the column wherein carbonate precipitates were present throughout the pore space (Fig. 5D).

3.3. Trends in aqueous chemistry and mineral saturation states

Rapid uptake of CO_2 into solution caused a spike in DIC concentration early in the experiments (Fig. 6A). Within 50 h these concentration peaks declined (stage 2). In 35% 2, DIC reached steady values between ~0.15 and 0.16 M within 50 and 100 h at the base and middle of the column, respectively (stages 3–4; Fig. 6A). In the 60% saturated column, on the other hand, DIC concentrations were highest in the middle of the column, fluctuating between 0.17 and 0.23 M (Fig. 6A). At the base of the column, after the transient peak at early time, the DIC slowly increased throughout the experiment, and did not reach a stable value (stage 2; Fig. 6A). This indicates that the base of the column was largely bypassed by CO_2 , in agreement with the gaseous CO_2 data.

Uptake of CO_2 into solution drives brucite dissolution (e.g., Harrison et al., 2013a; Hövelmann et al., 2012b; Pokrovsky et al., 2005; Zhao et al., 2010), and not surprisingly, Mg concentrations followed a similar trend as DIC concentrations (Fig. 6C). Rapid initial increases within 24 h were followed by a gradual reduction (stages 1–3). Mg concentrations

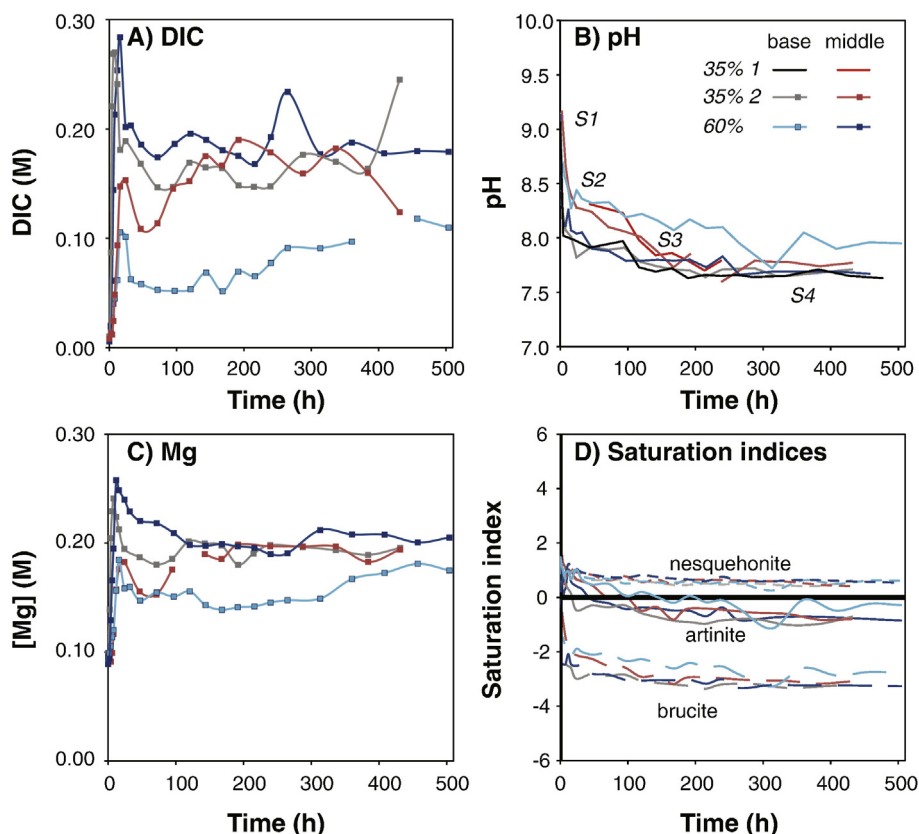


Fig. 6. Aqueous chemistry data versus time. A) Dissolved inorganic carbon (DIC) concentrations, B) pH, and C) Mg concentrations versus time. D) Mineral saturation indices versus time as calculated using PHREEQC (Parkhurst and Appelo, 2013) with the Pitzer database and mineral solubility data from the minteq database. Light red and gray lines and squares represent data from the middle and base of 35% 2, respectively. Dark blue and light blue lines and squares represent data from the middle and base of the 60% saturated column, respectively. The black and bright red lines in (B) represent the base and middle of 35% 1, respectively. In (D), the long and short dashed lines represent the saturation indices of brucite and nesquehonite, respectively, and the solid lines represent the saturation index of artinite.

stabilized at ~0.2 M within 120 h at both sampling locations in 35% 2, and in the middle of the 60% saturated column (stage 4; Fig. 6C). At the base of the 60% saturated column, an early transient peak was followed by a slow increase in Mg concentration for the remainder of the experiment (Fig. 6C).

The pH in the system is controlled by the balance between CO_2 dissolution, which decreases pH, and brucite dissolution, which increases pH. As such, the rapid DIC uptake was accompanied by a decline in pH in all columns (Fig. 6B; stages 1–2). The pH values declined from an initial value of 9.1 in all columns to ~8.0 within 12 h at the base of the 35% saturated columns. In the middle of these columns, the pH dropped rapidly to ~8.3 within 24 h, after which the rate of decline slowed considerably (stage 3; Fig. 6B). Final pH values were fairly stable at 7.6–7.8 at both locations (stage 4). The 60% saturated column exhibited a unique trend; the pH at the middle of the column followed a similar development as the base of the other columns, whereas the base sustained a higher pH throughout (~8.0–8.3; Fig. 6B). This is attributed to CO_2 largely bypassing this sampling zone due to preferential flow along a different pathway.

Mineral saturation indices (SI) were calculated from the aqueous chemistry data using PHREEQC (Parkhurst and Appelo, 2013). Prior to initiation of the CO_2 supply, the solutions were moderately undersaturated with respect to brucite ($\text{SI} = -0.5$ to -0.7). DIC uptake rapidly drove the solutions to be highly undersaturated with respect to brucite ($\text{SI} = -1.5$ to -3.4), and supersaturated with respect to both nesquehonite and artinite (Fig. 6D). Nesquehonite remained slightly supersaturated (0.1 to 1.2) throughout the experimental duration, whereas artinite became undersaturated after 100 h ($\text{SI} = -0.1$ to -1.1 ; Fig. 6D).

3.4. Water and gas flow

Although a gradient in gas phase pressure must have existed to drive the gas flux through the columns, differences in gas phase pressure were too low to be resolved within measurement error (± 23.2 Pa), and remained circum-atmospheric. In all columns the water content was lowest at the top of the column (~15% saturated) and highest at the base (close to 100% saturated; Fig. 4). Because the supplied gas was not humidified, it is expected that water was lost due both to evaporation and precipitation of hydrated Mg-carbonates. However, the volumetric water content sensors did not resolve significant changes in water saturation at any of the three measurement depths (SM Fig. 3B). Conversely, estimates of the total water mass in the columns, as calculated gravimetrically for the entire mass of the porous medium at the end of the 35% 2 and 60% saturated experiments, indicated that up to ~30% of the initial water was lost in these columns. As some solid material and pore water was lost during deconstruction of the experimental apparatus, some of the final pore water was not accounted for; thus this estimate is an upper limit to the water loss during the experiment. The discrepancy between these two measurements suggests either that hydraulic redistribution allowed replenishment of water at the sensor locations, or that reaction induced water loss was localized and did not significantly change the water saturation measured in the vicinity of each sensor.

3.5. Stable carbon isotope fractionation

The change in stable carbon isotopic composition of the gaseous CO_2 and dissolved inorganic carbon was tracked both temporally

and spatially within the columns. The supplied gas had a $\delta^{13}\text{C}$ value of $-36.6 \pm 0.1\text{‰}$ in all experiments, with slight variation between experiments due to the use of different CO_2 tanks. Enrichment in $\delta^{13}\text{C}$ values of the supplied gas of $0.7 \pm 0.4\text{‰}$ was documented between duplicate samples from the beginning and end of the 35% 2 experiment, owing to the use of a liquid CO_2 tank with an evolving stable isotopic composition. The same change in supplied gas composition was assumed for all experiments. Gases could not be sampled from the base of the experiments owing to the high water content, whereas water could not be sampled from the top of the columns due to the low water content. In addition, gas samples collected from the middle and top of the columns for at least the first 47 h of the experiments had insufficient CO_2 content to analyze.

Progressive depletion of ^{13}C in the supplied gas along the flow path is evident in both datasets, and is consistent with Rayleigh fractionation due to removal of CO_2 from the gas stream and its sequestration in carbonate minerals (Fig. 7A). The expected evolution of the stable isotopic composition of gaseous CO_2 based on Rayleigh fractionation was calculated assuming that the supplied gas had a constant composition equal to that of the tank CO_2 composition at the end of each experiment. A gas–solid fractionation factor based on the $\text{CO}_2\text{--HCO}_3^-$ fractionation factor of Mook et al. (1974) for the average temperature of each experiment, and the HCO_3^- dypingite [$\text{Mg}_5(\text{CO}_3)_4(\text{OH})_2 \cdot 5\text{H}_2\text{O}$] fractionation factor of Wilson et al. (2010) at 21°C was used. The temperature dependence of the latter has not been determined. The fractionation factor between HCO_3^- and nesquehonite or pseudo-artinite is unknown, however, the equilibrium fractionation factor of Wilson et al. (2010) was found to be consistent with fractionation observed during precipitation of nesquehonite under similar experimental conditions (Harrison et al., 2013a), justifying its use here. The gas phase CO_2 concentration sensors were used to calculate the extent of conversion (i.e., sequestration) of the gas phase along the flow path over time. The relatively good agreement of the experimental results with the gas–solid fractionation factor implies that the water provided a negligible reservoir for CO_2 on the timescale of the reaction, as is consistent with DIC measurements. For example, in the 35% 2 experiment, it is estimated that ~ 6 h would be required to completely replace the aqueous DIC with “fresh” CO_2 from the gas phase, compared to a > 150 h reaction time. Moreover, the rapid reduction of DIC concentrations towards steady-state values within the first 100 h of the experiments suggests it was rapidly incorporated into the solid phase. The presence of preferential flow paths in the 60% saturated experiment resulted in poor agreement between the modeled and experimental data at early time (Fig. 7A) because the gas samples accessed a larger volume of gas than was measured by the CO_2 concentration sensor from which the Rayleigh curve was calculated.

Throughout the experimental duration, $\delta^{13}\text{C}_{\text{DIC}}$ values were in general relatively enriched compared to the Rayleigh fractionation model for all experiments, but followed the predicted trend (Fig. 7B). Significant discrepancy between modeled and experimental data was documented at early time, owing to the presence of $\leq 1.5 \times 10^{-2} \text{ mol L}^{-1}$ initial DIC with $\delta^{13}\text{C}$ values between -12.6‰ and -10.1‰ that was not accounted for in the Rayleigh model. Upon initiation of the gaseous CO_2 supply, the $\delta^{13}\text{C}_{\text{DIC}}$ plummeted rapidly as the comparatively ^{13}C -depleted gaseous CO_2 dissolved into solution (Fig. 7B), and continued to evolve in a manner consistent with Rayleigh fractionation of the supplied gas along the flow path (Fig. 7B).

The stable isotopic composition of the solid carbonate phases represents a cumulative signature developed over time, as samples could only be collected at the end of the experiments. The $\delta^{13}\text{C}$ values of the secondary carbonate phases were calculated from measured bulk values of all solids by correcting for the contribution from dolomite present in the initial brucite ore. The dolomite abundance was quantified in aliquots of each sample using XRD data collected at the end of the experiments. The $\delta^{13}\text{C}$ value of the initial carbonates was $-6.5 \pm 0.3\text{‰}$ as measured in triplicate unreacted samples. Although magnesite and hydromagnesite were also documented in the initial brucite ore, they were not present at sufficient abundance in the reaction products to be quantified, however this initial ^{13}C composition was assumed representative of the remaining dolomite. Due to the error associated with the corrections for the initial carbonate, the uncertainty in the $\delta^{13}\text{C}$ values of the secondary carbonate phases is considerable and difficult to quantify. Nevertheless, they are broadly consistent with equilibrium fractionation between DIC and hydrated Mg-carbonates (Fig. 7B), as has been observed previously under similar experimental conditions (Harrison et al., 2013a; Wilson et al., 2010).

4. Reaction processes

The observed trends in CO_2 breakthrough curves are manifestations of reaction rate and progress along the length of the columns. Importantly, the reasonably constant $p\text{CO}_2$ measured during stage 2 reveals that reaction rates remained relatively constant at all column depths for ~ 85 h in the 35% saturated experiments and ~ 50 h in the 60% saturated experiment (Fig. 8A–C). The $p\text{CO}_2$ plateau occurred at similar timing and for similar durations at all three measurement locations within any single experiment (Fig. 8B and C). A precipitous cessation of carbonation following stage 2 is evidenced by the broader range in CO_2 sequestration rate and CO_2 concentration during stage 3 at each measurement depth within the columns (Fig. 8B and C), and the consistent approach towards the CO_2 concentration of the supplied gas ($C/C_0 \rightarrow 1$; Fig. 8A). Finally,

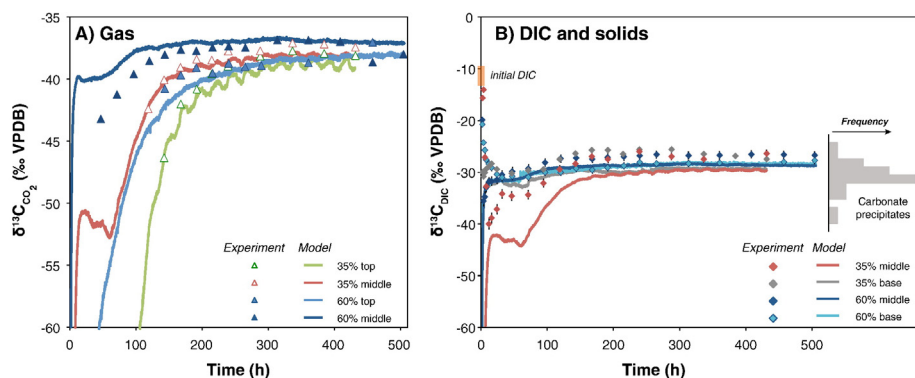


Fig. 7. Stable carbon isotopic composition of gaseous CO_2 , dissolved inorganic carbon (DIC), and secondary carbonate solid phases. All $\delta^{13}\text{C}$ values are reported in δ -notation relative to Vienna Pee Dee Belemnite (VPDB) in units of per mil (‰). A) Measured (points) and Rayleigh modeled (lines) $\delta^{13}\text{C}$ values of gaseous CO_2 versus time. B) Measured (points) and Rayleigh modeled (lines) $\delta^{13}\text{C}_{\text{DIC}}$ values versus time and $\delta^{13}\text{C}$ values of secondary solid carbonate phases, expressed as $\delta^{13}\text{C}_{\text{DIC}}$ equivalent using the fractionation factor of Wilson et al. (2010). Solid compositions are plotted as a histogram with frequency on the y-axis and $\delta^{13}\text{C}_{\text{DIC}}$ on the x-axis for a total of 29 samples. The orange shaded region represents the range of composition of initial DIC prior to initiation of the gaseous CO_2 supply.

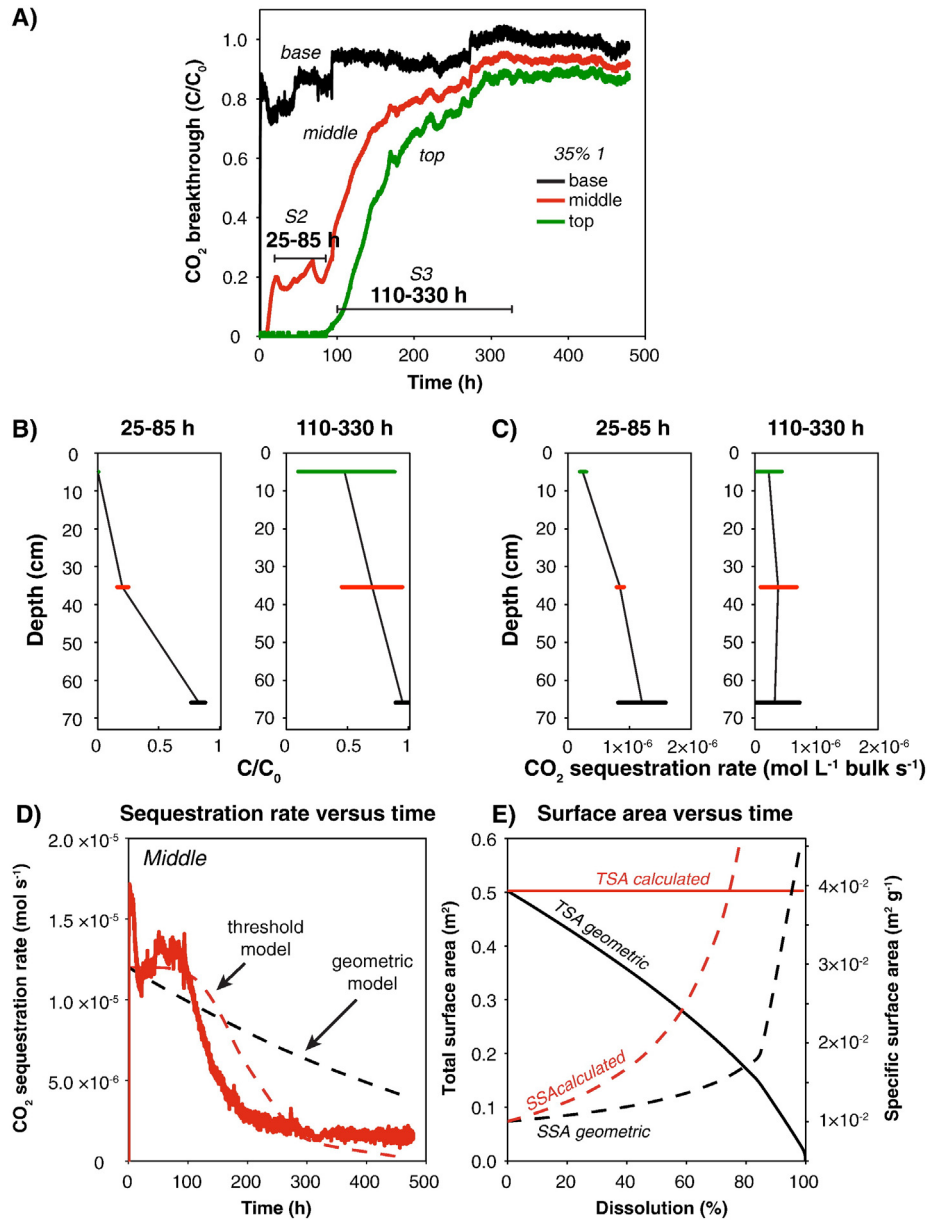


Fig. 8. Analysis of CO₂ breakthrough curve features. A) CO₂ breakthrough curves from 35% 1. Black, red, and green lines represent CO₂ concentration measurements at the base, middle, and top of the column. CO₂ breakthrough is expressed as C/C₀, the ratio of the measured CO₂ concentration at a given time to the CO₂ concentration of the supplied gas. B) C/C₀ versus depth in 35% 1 during reaction stage 2 (25–85 h) and reaction stage 3 (110–330 h). C) CO₂ sequestration rate versus depth in 35% 1 during reaction stage 2 (25–85 h) and reaction stage 3 (110–330 h). Rates were calculated using the CO₂ flux data at each sensor and are expressed as mol CO₂ L bulk⁻¹ s⁻¹. For both (B) and (C), horizontal bars represent the range in value of C/C₀ or CO₂ sequestration rate at a given depth for the entire time range plotted. Data are averaged over 2 h intervals (25 measurements) to reduce measurement noise. D) Comparison of the experimental instantaneous reaction rate (solid red line) versus time in the middle of the column and the reaction rates predicted by the geometric (dashed black line) and threshold (dashed red line) models. E) Calculated evolution of total surface area and specific surface area versus extent of brucite dissolution. Solid and dashed black lines show the evolution of total and specific reactive surface area, respectively, as calculated using the geometric model. The solid red line shows the total surface area evolution required to maintain a constant reaction rate, and the dashed red line shows the evolution of specific surface area required to achieve this constant total surface area. (For interpretation of the references to color in this figure legend, the reader is referred to the web version of this article.)

in the 60% saturated column, the CO₂ breakthrough curves measured at the middle and base of the column are remarkably similar, implying that no significant reaction was occurring between these two measurement points for most of the experimental duration. These features of the breakthrough curves are important indicators of the reaction processes governing carbonation during the different stages of reaction.

4.1. Evolution of reactive surface area

4.1.1. Surface area generation

It is typically expected that bulk mineral dissolution rates decline over time as the reactive phase is consumed, due to the geometric

reduction in particle size and consumption of reactive surface area (Appelo and Postma, 2005; Levenspiel, 1999). This decline in surface area is often approximated with the following relationship representative of a uniform population of shrinking spheres or cubes (Appelo and Postma, 2005; Colón et al., 2004; Jeon et al., 2007; Lichtner, 1996; Mayer et al., 2002; Wilson et al., 2014), referred to as the “geometric model:”

$$k_{eff}^g = k^0 SA \left(\frac{\varphi^t}{\varphi^0} \right)^{2/3} \quad (3)$$

where k_{eff}^g (L s⁻¹) is the effective “geometric” rate constant, k^0 is the initial reaction rate constant equal to 10^{-6.13} L s⁻¹ m⁻²

(after Pokrovsky et al., 2005), SA is the surface area (m^2), and φ^0 and φ^t are the volume fraction of the reactive phase initially and a given time greater than zero, respectively. Here, k_{eff}^g replaces k_{eff}^0 in Eq. (1). Such a relationship results in a gradual decline in reaction rate associated with the shrinking geometric surface area of the particles, and is in poor agreement with the experimental observations (Fig. 8D). Rather, a period of constant reaction rate (stage 2; Fig. 8B) suggests either that the effective surface area of brucite remains relatively constant despite its consumption, or that the overall sequestration rate is not controlled by brucite dissolution kinetics. The latter implies that either the supply of CO_2 or the rate of carbonate precipitation was limiting the overall reaction rate. The advancement of a sharp reaction front through the columns could also produce a constant bulk rate of reaction, but the presence of contemporaneous gas composition plateaus throughout the column disqualifies this as an explanation (Fig. 8A–C).

A constant reaction rate would be achieved if the rate-limiting step for carbonation were the supply of CO_2 , as the sequestration rate would approximately balance the supply rate. However, the elevated CO_2 concentration throughout most of the column depth (Fig. 8A and B) implies that CO_2 gas is supplied to the column faster than it is locally removed. Other studies have shown that the gas-solution transfer and subsequent hydration of aqueous CO_2 to a form that can be mineralized may be relatively slow compared to the flux of CO_2 gas (Harrison et al., 2013a; Power et al., 2013a; Wilson et al., 2010). This would result in effectively CO_2 -limited brucite carbonation despite the non-zero CO_2 concentration in the gas phase. CO_2 uptake into solution has been demonstrated to be rate limiting under similar experimental conditions (Harrison et al., 2013a; Power et al., 2013a; Wilson et al., 2010), and is typified by anomalously depleted ^{13}C compositions of both DIC and precipitated carbonates due to kinetic fractionation of stable carbon isotopes during uptake of CO_2 into solution (Harrison et al., 2013a; Wilson et al., 2010, 2014). However, there is no evidence for this kinetic fractionation effect in the column experiments; the stable carbon isotopic compositions can be explained by a Rayleigh effect (Fig. 7). Furthermore, deviations from the ideal Rayleigh effect tended towards ^{13}C -enrichment compared to model values (Fig. 7B), whereas kinetic fractionation during CO_2 uptake would have the opposite effect. This suggests that CO_2 uptake into solution was not rate limiting. The discrepancy between these and previous experimental results (Harrison et al., 2013a; Wilson et al., 2010) is attributed to the use of different experimental apparatus. Previous studies that identified CO_2 uptake as the rate-limiting step were conducted in batch reactors; the increased gas–water interface provided in the column experiments likely facilitated more rapid uptake of CO_2 into solution. Thus it appears unlikely that the overall reaction rate was limited by the rate of CO_2 supply.

Changes in total brucite surface area would also have less of an impact on the bulk rate of CO_2 sequestration if carbonate precipitation were to limit the overall carbonation rate, a limitation which has recently been recognized for certain carbonation reactions (e.g., Gautier et al., 2014; Hövelmann et al., 2012a; Kampman et al., 2014; Pham et al., 2011; Saldi et al., 2012). A relatively slow rate of secondary phase precipitation may in some cases allow the solution to approach equilibrium with respect to the dissolving phase, retarding its dissolution (Maher et al., 2009). The moderate supersaturation with respect to nesquehonite documented in the columns (Fig. 6) implies that its precipitation was moderately kinetically inhibited. Nevertheless, brucite remained undersaturated in the bulk solution (saturation index ≈ -0.5 to -3.4 ; Fig. 6), implying that reaction affinity effects due to relatively slow carbonate precipitation were unlikely to have limited the CO_2 sequestration rate. Furthermore, pH values tended to plateau contemporaneously with CO_2 concentrations, implying that a quasi-steady-state is achieved between brucite dissolution and carbonate precipitation. Because the reactions are sequential, the observed quasi-steady-state implies that brucite dissolution controls the overall reaction rate during stage 2 of the reaction.

Our smaller scale experiments revealed that an increase in brucite surface area accelerated the carbonation reaction under similar experimental conditions (Harrison et al., 2015), implying that brucite dissolution was the rate-limiting step. In order to maintain the relatively constant rate of reaction during stage 2, the implication is that the total available brucite surface area remained relatively constant despite the net loss of brucite mass. This is inconsistent with the hypothesis that surface area evolves according to the geometry of a shrinking cubic or spherical particle (Fig. 8D). A geometric model allows the total surface area of the reacting phase to decline as the phase is consumed, despite an increase in the surface area per unit mass (specific surface area; Fig. 8E). It is recognized that the reactive surface area of a mineral is not always equal to the geometric surface area, in which case it should not be expected to evolve geometrically. Surface roughness and mesoporosity provide additional surface area that is not accounted for by simple geometric models (e.g., Brantley and Mellot, 2000). Moreover, not all surface area is equally reactive (e.g., Gautier et al., 2001). For example, the crystal edges of several sheet silicate minerals dissolve much more rapidly than basal sheets (Bickmore et al., 2001; Bosbach et al., 2000; Hodson, 2006), as do edge dislocations associated with exsolution lamellae (Lee et al., 1998) and defects induced by grinding (Maher et al., 2006; Petrovich, 1981; White and Brantley, 2003). In the case of brucite, the relatively constant reaction rate recorded during stage 2 implies that the specific surface area (i.e., surface area per unit mass) must be increasing non-geometrically to account for the loss of brucite mass (Fig. 8E). Moreover, the particles must consistently maintain exposure to water during this time.

Although brucite surface area could not be reliably measured post-reaction due to the intergrown nature of the carbonate precipitates with the residual brucite, there are three plausible mechanisms by which surface area could be generated or maintained that are consistent with experimental observations. First, surface area may be maintained if reaction occurred primarily via the stepwise removal of $Mg(OH)_2$ sheets, such as observed during brucite dissolution by Hövelmann et al. (2012b) at the nano-scale using atomic force microscopy. If the majority of reaction occurred in this manner, with little reaction on particle edges, the total reactive surface area may not change substantially with reaction progress, as the surface area of each newly exposed sheet would be similar throughout the reaction. Similarly, it has been documented that transformations between sheet silicates can proceed via the replacement of individual layers, such as during replacement of anthophyllite by talc (e.g., Veblen and Ferry, 1983). The observation of thin brucite remnants completely surrounded by carbonate precipitates could be attributed to a similar reaction mechanism (Fig. 5F), which would allow increased exposure of 'interior' brucite surface area. Alternatively, surface area may be generated due to reaction-induced fracturing of the brucite grains, owing to the large difference in density between products and reactants (Kelemen et al., 2011 and references therein). For example, Beinlich and Austrheim (2012) documented that precipitation of lansfordite fractured serpentinite clasts during weathering. The presence of carbonate-filled cracks that extend well within brucite grains (Fig. 5B) may be indicative of this process. The 'force of crystallization' may be calculated as a function of the saturation state of the precipitating phase (e.g., Beinlich and Austrheim, 2012; Scherer, 2004). Here, we estimate that up to ~ 40 MPa of pressure could be generated by nesquehonite precipitation based on the saturation indices calculated using PHREEQC (Parkhurst and Appelo, 2013; refer to SM for force of crystallization calculations). Considering the typical tensile strength of rock is in the range of 5 to 10 MPa (Etheridge, 1983), it is plausible that sufficient force was generated during carbonation to fracture brucite grains. Finally, the increase in surface area may be due to preferential dissolution along weaknesses in the particles, which may have been induced during pulverization of the initial brucite ore. Similar to reaction-induced cracking, this may also lead to the development of carbonated channels that extend into the interior of reacted brucite grains (Fig. 5B). Intragranular dissolution along planes

can also lead to physical weakening of the mineral grain, which induces flaking and exposure of fresh surface area (Lee et al., 1998). The observed brucite pieces separated from the surface and isolated between extensive carbonate precipitates could be attributed to this process (Fig. 5E and F), which is likely facilitated by the basal cleavage of brucite. Although the data are not sufficient to distinguish absolutely between the three mechanisms proposed, the observed textures unmistakably illustrate that the evolution of reactive surface area was highly non-geometric, and therefore cannot be predicted using a simple geometric model. The observed fracturing and fragmentation of brucite particles would counteract the reduction in brucite mass as the reaction progressed, permitting the observed relatively constant rate of reaction (Fig. 8E).

4.1.2. Surface passivation

Our previous experimental results from smaller scale brucite carbonation columns revealed that the transformation from a flakey, poorly or nano-crystalline carbonate phase to low porosity, bladed nesquehonite resulted in abrupt passivation of brucite and arrested the reaction (Harrison et al., 2015). The morphology and stoichiometry of the poorly crystalline phase was similar to that of the pseudo-artinite in the present study. Due to the stoichiometric similarity between artinite and the pseudo-artinite formed in the experiments, artinite solubility data are used as a proxy for pseudo-artinite in all models. Aqueous chemistry data, which were not available from the smaller scale experiments, revealed that although nesquehonite quickly became supersaturated and remained so throughout the experiment, artinite became undersaturated within 100 h due to the decline in pH (Fig. 6D). The change in saturation state of artinite with time and the constant supersaturation with respect to nesquehonite are consistent with initially rapid precipitation of pseudo-artinite, coupled with relatively slow precipitation of nesquehonite replacing the earlier-formed carbonate. The observation of bladed crystals rimming pseudo-artinite supports this interpretation (Fig. 5A). A similar phase transformation has been observed in batch experiments, wherein chlorartinite $[\text{Mg}_2(\text{CO}_3)\text{Cl}(\text{OH}) \cdot 3\text{H}_2\text{O}]$ is an intermediate phase that is replaced by nesquehonite (Kristova et al., 2014). The transformation from porous pseudo-artinite to low porosity nesquehonite as the chemical environment evolved resulted in abrupt passivation of the brucite surface. The coincidence of the reaction shut down and transition from artinite saturated to under-saturated conditions demonstrates that the surface passivation process is attributable to the carbonate phase transformation rather than a porosity threshold associated with a certain extent of carbonate precipitation, a distinction we were unable to make with our previous experimental data (Harrison et al., 2015).

4.1.3. Threshold model

The geometric model does not account for surface area generation and surface passivation, thus it cannot be used to predict reaction progress in the experimental systems (Fig. 8D), nor for similar reactions at field scale. Instead, we developed an empirical model, referred to as the “threshold model” based on the results of our previous, smaller scale column experiments (Eq. (4); Harrison et al., 2015).

$$k_{\text{eff}}^t = k^0 SA \left[1 - \left(\frac{\varphi^0 - \varphi^t}{\varphi^0 - \varphi^p} \right)^5 \right] \quad (4)$$

for $\varphi^t \leq \varphi^p$, where k_{eff}^t is the effective “threshold” rate constant (L s^{-1}), k^0 is the initial reaction rate constant equal to $10^{-6.13} \text{ L s}^{-1} \text{ m}^{-2}$ (after Pokrovsky et al., 2005), SA is the brucite surface area (m^2), and φ^0 and φ^p are the initial brucite volume fraction and a threshold brucite volume fraction at which the reaction rate becomes negligible due to surface passivation. Here, k_{eff}^t replaces k_{eff}^0 in Eq. (1). This model allows for a relatively constant rate of reaction at early time, owing to the previously unrecognized surface area generation effects, followed

by a rapid shutdown at an empirically determined threshold of conversion (φ^p), as associated with surface passivation effects. Due to the similar behavior observed in both the small and large column experiments, the threshold model was employed in MIN3P-DUSTY (Mayer et al., 2002; Molins and Mayer, 2007) to simulate the experimental conditions of 35% 1. The 60% saturated column was not modeled, as preferential gas flow and the associated extreme spatial heterogeneity in reaction extent implies that our uniform one-dimensional model is insufficient. For further detail regarding the model setup, please refer to the Supplementary Material.

It was found that the threshold model reproduced our experimental results reasonably well for the wetter base and middle of the column (Fig. 9B), but the mass of CO_2 sequestered was significantly overestimated for the upper, dry regions of the column (Fig. 9). This overestimation implies that a process other than, or in addition to, surface passivation limits the extent of carbonation achieved in the drier, upper areas of the columns. Moreover, this confirms that the reduced amount of carbonation near the tops of the columns is not simply a result of being further from the CO_2 source.

4.2. Water limited reaction

Water is required both as a reaction medium that facilitates CO_2 and brucite dissolution as well as a reactant that is incorporated into the crystal structures of the hydrated Mg-carbonate products. It is therefore hypothesized that the water content of porous media may exert an important influence on reaction progress. The consistently lower extent of reaction recorded in the drier regions of the columns and the failure of the threshold model to reproduce our experimental results for these areas of the column (Figs. 4 and 9) are in agreement with this hypothesis. Similarly, in our previous smaller scale experiments, only ~35% of the brucite was carbonated in a 15% saturated experiment in contrast to ~60% carbonation achieved in 35% and 50% saturated experiments (Harrison et al., 2015). The apparent correlation between the mass of carbon sequestered and the abundance of nesquehonite with bulk water saturation (Fig. 4) suggests that both overall carbonation extent and mineral phase transformations may be governed by the availability of water. In addition, the observation that the CO_2 breakthrough curves are similar at the base of the 35% and 60% saturated columns, where the water saturations are comparable, but the curves are different at the middle and top of the columns, where water saturations differ more strongly between columns (Fig. 4D), highlights that water saturation is a strong control on bulk reaction rate.

The precipitation of hydrated Mg-carbonate phases at ambient temperature imposes a fundamental limit to the mass of carbonate that can form according to the stoichiometry of the carbonate and the total mass of water in the system. In the case of brucite carbonation to form nesquehonite, two moles of water are required per mole of carbonate formed, compared to 1 mole of water per mole of pseudo-artinite. Moreover, the transition from pseudo-artinite to nesquehonite consumes water (Eq. (5)).



Gravimetric measurements of the final water content distribution in the columns revealed that a sufficient volume of water is available to allow complete transformation from brucite to nesquehonite throughout the 60% saturated column, and in all but the top 10 cm of the 35% saturated columns. Still, the bulk volume of water available in this upper region should be sufficient to allow ~80–99% reaction, compared to a measured maximum of ~29% reaction in this zone. This suggests that the reduced carbonation and phase transformation at lower water saturation is not simply a stoichiometric effect. Instead, it may relate to the role of water as a reaction medium rather than as a reactant.

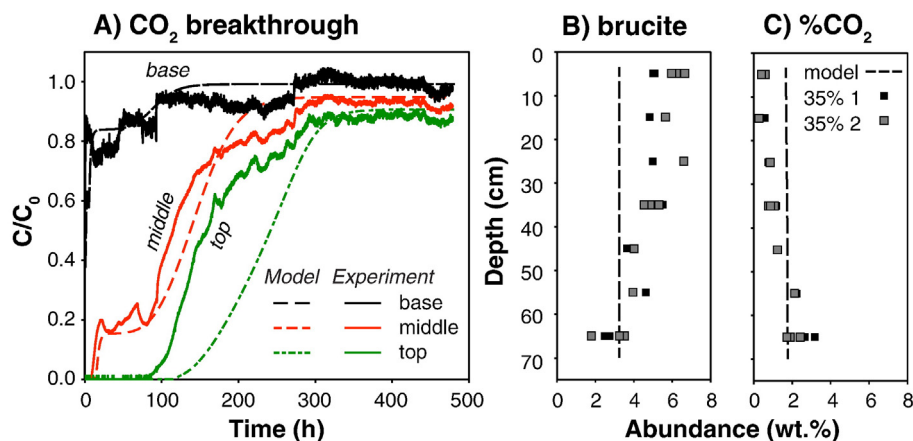


Fig. 9. Comparison of modeled and experimental data. A) Modeled versus experimental CO₂ breakthrough curves from 35% 1. Black, red, and green lines represent CO₂ breakthrough curves from the base, middle, and top of the column. Solid and dashed lines represent experimental and modeled data, respectively. B) Modeled and measured secondary phase solid CO₂ abundance versus depth. C) Modeled and measured secondary phase solid CO₂ abundance versus depth. In both (B) and (C), the black and gray squares illustrate measured values from 35% 1 and 2, respectively. The dashed line represents the model output. (For interpretation of the references to color in this figure legend, the reader is referred to the web version of this article.)

Heterogeneous water distribution at the pore scale may leave some mineral surfaces relatively unexposed to reactive fluids, reducing the surface area available for reaction. In natural systems, it has been observed that the solute flux is governed by the water table elevation – in effect the quantity of mineral surface area exposed to water (Eiriksdottir et al., 2013). Thus, the lack of carbonation may be attributable to poor exposure of brucite surfaces to water. At low water saturation, water is held primarily in pore throats and as thin films

coating mineral surfaces rather than in large pores, hence it is relatively immobile. The consumption of water during precipitation of pseudo-artinite may sufficiently diminish the local water volume in a pore throat or water film such that the phase transformation cannot proceed, despite the bulk volume being in excess of that required by stoichiometry. Alternatively, it has been observed that reaction of brucite, forsterite [Mg₂SiO₄], and wollastonite [CaSiO₃] with wet supercritical CO₂ (Felmy et al., 2012; Loring et al., 2011; Miller et al., 2013; Schaefer

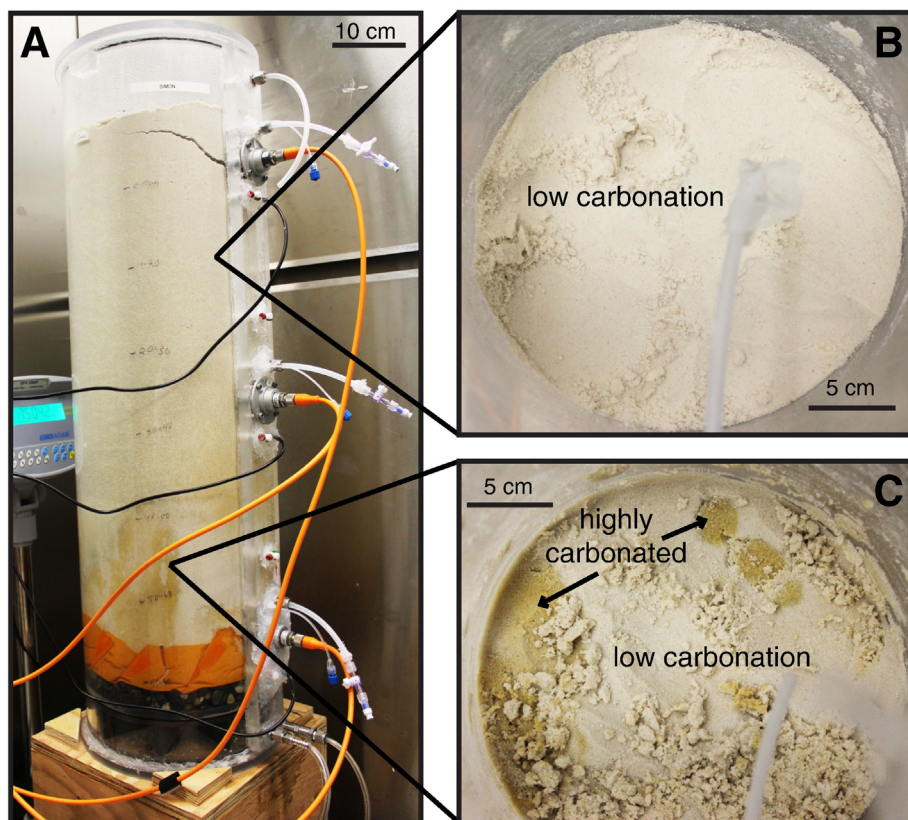


Fig. 10. Photograph of the 60% saturated column at the conclusion of the experiment. A) Photograph of the column exterior at the conclusion of the experiment showing reaction fingers – narrow zones of highly reacted material typified by an orange coloration. Off-white areas are zones of poorly carbonated material. The bright orange area seen from the exterior at the column's base is the mesh that separates the reactive material from the gravel layer. Map view of the solid materials at the conclusion of the experiment during excavation near the top of the column (B) and near the base of the column (C). Orange colored reaction fingers are evident near the base of the column, but are not visible near the top of the column due to the overall lesser extent of reaction, which was insufficient to induce a visible color change. (For interpretation of the references to color in this figure legend, the reader is referred to the web version of this article.)

et al., 2011) requires a certain threshold water saturation to proceed. If similar behavior occurs for gaseous CO₂, the implication is that simply being exposed to water may not facilitate reaction in itself; rather, a certain volume is required to facilitate complete reaction. Schaefer et al. (2011, 2013), for instance, documented that forsterite carbonation in wet supercritical CO₂ ceases when water films are too thin to behave like bulk water, and that brucite carbonation is arrested prior to completion due to water loss to nesquehonite. Finally, it is possible that the solubility of the gaseous and mineral phases are altered under the negative, capillary pressures experienced in the unsaturated zone (e.g., Pettenati et al., 2008), such that reaction progress does not occur as expected. However, the impact of negative pressure on the solubility of brucite and nesquehonite is not known, preventing further assessment of this hypothesis.

4.3. Preferential flow paths

The anomalously early breakthrough documented at the middle sensor of the 60% saturated column, and the heterogeneity in reaction extent in all columns is indicative of preferential flow paths. Orange coloration visibly identifies narrow (~5 cm diameter) channels of highly reacted material surrounded by white, low to moderately carbonated material (Fig. 10A and C). Although some channeling was observed in the 35% saturated columns, the process was most pronounced in the 60% saturated column. This is attributed to the higher percentage of water filled pores that effectively block gas transport (Collin and Rasmuson, 1988); therefore a reduced volume is available for gas flow. Because the bases of the columns were at or close to 100% water saturation, gas flow into the columns necessitated displacement of pore water. This may trigger the development of viscous fingers in the direction of flow and thus heterogeneous distribution of the invading fluid in the porous medium (Hill, 1952; Kueper and Frind, 1988; Marulanda et al., 2000). Although the importance of viscosity and density differences has been demonstrated in homogeneous media (Marulanda et al., 2000 and references therein), in physically heterogeneous porous media, viscous fingering becomes less important, and flow paths are instead governed by the heterogeneous permeability field (Kueper and Frind, 1988). It is highly likely that small-scale physical heterogeneities in the porous medium lead to preferential channelization of the flow along more permeable paths in addition to the effects of viscous fingering.

Although initial intrinsic and relative permeability distributions are likely to control the early infiltration of the porous medium by the gas phase, the question as to how these initial fingers will evolve during carbonation due to reaction induced changes in porosity and permeability provides additional complexity. Mineral dissolution and precipitation can lead to positive or negative feedbacks that enhance or dampen finger development; a process known as reactive-infiltration instability (e.g., Daccord and Lenormand, 1987; Daccord, 1987; Dipple and Gerdes, 1998; Kalia and Balakotaiah, 2007; Kelemen et al., 1995; Ortoleva et al., 1987). Despite the removal of water from the pore space during hydrated Mg-carbonate precipitation, a net decrease in gas-filled pore volume during carbonation is expected due to the large solid volume increase, irrespective of the type of Mg-carbonate mineral formed (SM Fig. S8). Yet, the persistence of the viscous fingers implies that permeability remained greater within the fingers than in the surrounding medium, despite the porosity reduction. This is attributed to the fact that precipitation would occur in water filled pores within the fingers (Harrison, 2014), thus the majority of pore space clogging would not occur in the gas-filled pores through which the gas was flowing. Moreover, the evaporative removal of water from the pore space would be greatest in the fingers where the gas flux was highest, thereby increasing the gas filled pore volume and relative permeability with respect to the gas phase; a positive feedback.

Due to the persistence of these preferential flow paths, a large proportion of the reactive material remained relatively unexposed to

CO₂, and therefore was poorly carbonated. As a result, the total mass of CO₂ sequestered was the least for the column with the highest bulk water saturation (60% saturated) despite the increased volume of water available for carbonation to proceed.

5. Implications

The distribution and evolution of mineral–water–gas interfacial area exerts a fundamental, but poorly understood, control on mineral–fluid reactions in the unsaturated zone. The water content and depth of the unsaturated zone may impact both the equilibrium fluid concentration and distance over which equilibration is achieved (“equilibration length;” Maher, 2011), and thus the solute flux derived from mineral weathering. The magnitude of the mineral–water–gas interfacial area is dictated by the bulk water content of the porous medium, the intrinsic mineral surface area, and the hydraulic properties of the porous medium. Our experiments show that an increased gas–water interfacial area facilitates the uptake of gas into solution, while the spatial distribution of gas–water interfaces and volume of water- versus gas-filled pore space controlled the extent of mineral reaction and distribution of precipitates.

Water saturation is likely to play an important role in the progress of mineral dissolution–precipitation reactions both in passive weathering systems and engineered environments with active gas flow. In either case, low water saturation may limit reaction progress and the solute flux. In particular, during engineered CO₂ sequestration, water saturation will strongly influence the mass of CO₂ stored. Low water saturation limits carbonate precipitation, and high water saturation encourages the development of preferential flow paths, limiting exposure of reactive phases to CO₂. If CO₂ were injected into a porous medium, this could in part be controlled by the rate of injection (e.g., Ji et al., 1993), periodic addition of water to “reset” preferential flow paths, and injection of gas only above the water table. The results of the column experiments imply that there is likely an optimum range of water content that facilitates maximum reaction progress both in natural and engineered environments in the shallow subsurface (i.e., with gaseous or aqueous CO₂ under near ambient pressure and temperature rather than CO₂ under elevated temperature and pressures conditions or in supercritical state), such as mine tailings or other alkaline waste stockpiles. Previous studies have revealed that in the case of carbonation of brucite or chrysotile mining residues, the ideal water content is between ~40 and 60% saturation (Harrison et al., 2015; Assima et al., 2013a), a conclusion that is consistent with the results of this study. The proportion of the unsaturated zone that is within this optimum range will be dictated by the material properties, with finer grained, poorly sorted materials maintaining ideal water saturation for a wider range of hydraulic suction (Fig. 11). The fine-grained nature of mine tailings, for example, may facilitate maintenance of a larger zone of ideal water content compared to a well-sorted sand (Fig. 11). Engineered strategies designed to maximize mineral reaction should therefore utilize fine-grained or poorly-sorted materials to optimize water retention.

The occlusion of both mineral reactive surface area and porosity via passivation and pore-clogging is also an important concern for CO₂ sequestration technologies that aim to mineralize carbon in porous media (e.g., saline or (ultra)mafic-hosted aquifers; Gherardi et al., 2007; Johnson et al., 2014; Kelemen and Matter, 2008; King et al., 2010; Luquot and Gouze, 2009; Peuble et al., 2015; Stockmann et al., 2011, 2013). Although extensive carbonate precipitation within water-filled pore space was observed in our experiments, preferential flow paths persisted throughout the entire experimental duration, implying that gas permeability can be maintained despite decreasing bulk porosity. At grain scale, areas with sufficient water supply were limited by brucite dissolution rates, and the brucite surface area exerted a direct control on the overall mineral carbonation rate. As reaction progressed, the brucite surface area

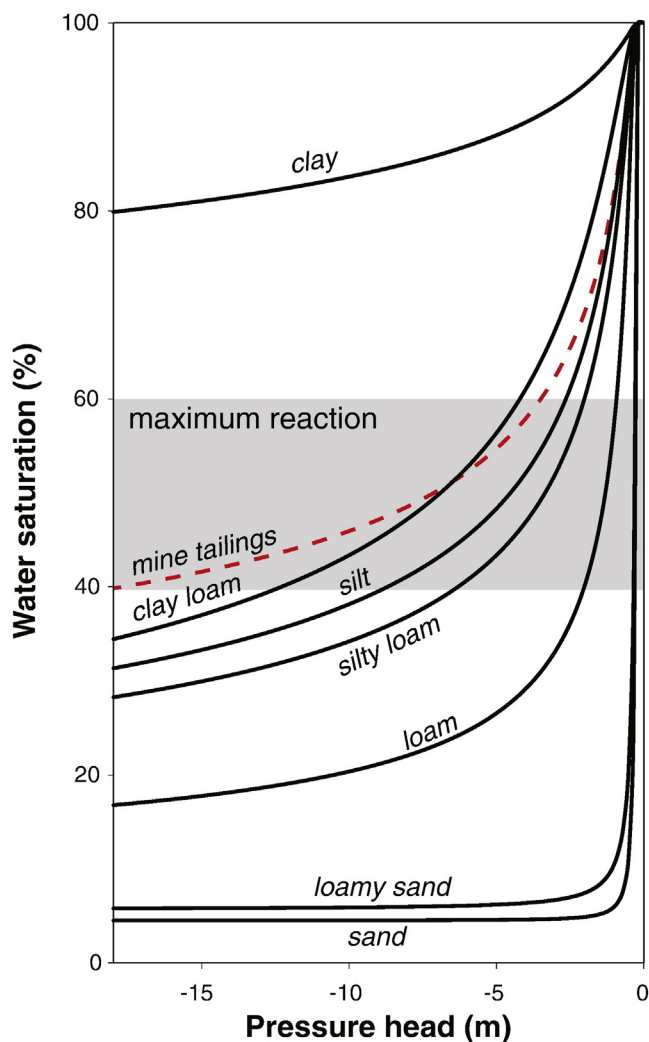


Fig. 11. Water saturation versus pressure head for different types of porous media. Water saturation was calculated for a 20 m sediment column in one dimension with a constant hydraulic head of 2 m, but variable pressure head, using MIN3P-DUSTY (Mayer et al., 2002; Molins and Mayer, 2007). Representative values for the soil water retention curves of the different porous media were taken from Hydrus 1-D (Šimůnek et al., 2013), except for mine tailings for which values were taken from Bea et al. (2012). The proposed ideal water content to allow maximum mineral–fluid reaction is illustrated by the shaded gray region. Finer-grained, poorly sorted materials, such as mine tailings, tend to remain within the proposed ideal water content range over the widest range of pressure head.

demonstrated a complex evolution including roughening, fracturing and passivation that is inconsistent with conventional models of geometric evolution. It has been posited that reaction-induced fracturing may help maintain reactive surface area during engineered carbonation of ultramafic rock in the subsurface (Kelemen et al., 2011), and this process has been invoked as an explanation for extensive carbonation and maintenance of permeability observed in the natural environment (e.g., Matter and Kelemen, 2009; Boschi et al., 2009). The textures of our experimental products were consistent with this process at the grain scale, demonstrating that it may also operate in near surface environments and help to maintain surface area during natural and engineered carbon mineralization reactions in the shallow subsurface (e.g., in mine tailings).

Conversely, the passivation processes associated with phase transformations between metastable precipitates could significantly reduce CO₂ sequestration efficiency. Similar phase transformations have been documented or inferred in natural and disturbed environments (Boschi et al., 2009; Power et al., 2014; Wilson et al., 2009), and may limit the extent of conversion of ultramafic and mafic material in the

shallow subsurface. The transition between hydrated phases is also relevant for Mg-sulfate, zeolite, and smectite minerals and may play an important role in the bioavailability of water (Bish et al., 2003; Wilson and Bish, 2012). Phase transformations in the Mg-carbonate system are known to be impacted by pH, temperature, and CO₂ and H₂O partial pressure (Hänchen et al., 2008; Hopkinson et al., 2012; Königsberger et al., 1999; Morgan et al., 2015). In fact, the phase transformation in our experiments appeared to be inhibited at low water saturation. Such environmental conditions could be tailored in engineered CO₂ sequestration strategies to minimize surface passivation.

Acknowledgments

This research was funded by a Carbon Management Canada National Centre of Excellence grant C390 to GMD and KUM, and a Natural Sciences and Engineering Research Council of Canada (NSERC) Discovery Grant to GMD. Research by ALH and IMP was supported by NSERC postgraduate and postdoctoral fellowships, respectively. We thank Timothy Mah, Maureen Soon, Charlie Wu, Paul Kenward, Gethin Owen, and Natasha Sihota for their analytical assistance. We are grateful to Jenine McCutcheon and Gordon Southam for providing XRF measurements, and thank Jörn Unger for constructing the columns. We thank David Jones and Pejman Rasouli for aid with LabView and MIN3P, respectively. This study benefited from discussion with Mark Johnson, Sasha Wilson, Andreas Beinlich, Natasha Sihota, Mati Raudsepp, and Sharon Blackmore. The manuscript also benefited from careful reviews from three anonymous reviewers.

Appendix A. Supplementary data

Supplementary data to this article can be found online at <http://dx.doi.org/10.1016/j.chemgeo.2015.12.005>.

References

- Appelo, C., Postma, D., 2005. *Geochemistry, Groundwater, and Pollution*. second ed. CRC Press, Amsterdam.
- Assima, G.P., Larachi, F., Beaudoin, G., Molson, J., 2012. CO₂ sequestration in chrysotile mining residues—implication of watering and passivation under environmental conditions. *Ind. Eng. Chem. Res.* 51, 8726–8734.
- Assima, G.P., Larachi, F., Beaudoin, G., Molson, J., 2013a. Dynamics of carbon dioxide uptake in chrysotile mining residues — effect of mineralogy and liquid saturation. *Int. J. Greenh. Gas Control* 12, 124–135.
- Assima, G.P., Larachi, F., Molson, J., Beaudoin, G., 2013b. Accurate and direct quantification of native brucite in serpentine ores—new methodology and implications for CO₂ sequestration by mining residues. *Thermochim. Acta* 566, 281–291.
- Barker, S.L.L., Dipple, G.M., Dong, F., Baer, D.S., 2011. Use of laser spectroscopy to measure the ¹³C/¹²C and ¹⁸O/¹⁶O compositions of carbonate minerals. *Anal. Chem.* 83, 2220–2226.
- Bea, S.A., Wilson, S.A., Mayer, K.U., Dipple, G.M., Power, I.M., Gamazo, P., 2012. Reactive transport modeling of natural carbon sequestration in ultramafic mine tailings. *Vadose Zone J.* 11.
- Beinlich, A., Austrheim, H., 2012. In situ sequestration of atmospheric CO₂ at low temperature and surface cracking of serpentinized peridotite in mine shafts. *Chem. Geol.* 332–333, 32–44.
- Berner, R.A., Lasaga, A.C., Garrels, R.M., 1983. The carbonate–silicate geochemical cycle and its effect on atmospheric carbon dioxide over the past 100 million years. *Am. J. Sci.* 283, 641–683.
- Bickmore, B., Bosbach, D., Hochella, M.F.J., Charlet, L., Rufe, E., 2001. In situ atomic force microscopy study of hectorite and nontronite dissolution: implications for phyllosilicate edge surface structures and dissolution mechanisms. *Am. Mineral.* 86, 411–423.
- Bish, D.L., William Carey, J., Vaniman, D.T., Chipera, S.J., 2003. Stability of hydrous minerals on the martian surface. *Icarus* 164, 96–103.
- Bobicki, E.R., Liu, Q., Xu, Z., Zeng, H., 2012. Carbon capture and storage using alkaline industrial wastes. *Prog. Energy Combust. Sci.* 38, 302–320.
- Bosbach, D., Charlet, L., Bickmore, B., Hochella, M.F.J., 2000. The dissolution of hectorite: in-situ, real-time observations using atomic force microscopy. *Am. Mineral.* 85, 1209–1216.
- Boschi, C., Dini, A., Dallai, L., Ruggieri, G., Gianelli, G., 2009. Enhanced CO₂-mineral sequestration by cyclic hydraulic fracturing and Si-rich fluid infiltration into serpentinites at Malenrata (Tuscany, Italy). *Chem. Geol.* 265, 209–226.
- Brantley, S.L., 2008. Kinetics of mineral dissolution. In: Brantley, S.L., Kubicki, J.D., White, A.F. (Eds.), *Kinetics of Water–Rock Interaction*. Springer, pp. 151–210.

- Brantley, S.L., Mellot, N.P., 2000. Surface area and porosity of primary silicate minerals. *Am. Mineral.* 85, 1767–1783.
- Collin, M., Rasmuson, A., 1988. A comparison of gas diffusivity models for unsaturated porous media. *Soil Sci. Soc. Am. J.* 52, 1559–1565.
- Colón, C.F.J., Oelkers, E.H., Schott, J., 2004. Experimental investigation of the effect of dissolution on sandstone permeability, porosity, and reactive surface area. *Geochim. Cosmochim. Acta* 68, 805–817.
- Daccord, G., 1987. Chemical dissolution of a porous medium by a reactive fluid. *Phys. Rev. Lett.* 58, 479–482.
- Daccord, G., Lenormand, R., 1987. Fractal patterns from chemical dissolution. *Nature* 325, 41–43.
- Daval, D., Martinez, I., Corvisier, J., Findling, N., Goffé, B., Guyot, F., 2009. Carbonation of Ca-bearing silicates, the case of wollastonite: experimental investigations and kinetic modeling. *Chem. Geol.* 265, 63–78.
- Dipple, G.M., Gerdes, M.L., 1998. Reaction-infiltration feedback and hydrodynamics at the skarn front. In: Lentz, D.R., Jambor, J.L. (Eds.), *Mineralized Intrusion-related Skarn Systems*. Mineralogical Association of Canada, Quebec City, Quebec, pp. 71–97.
- Eiriksdottir, E.S., Gislason, S.R., Oelkers, E.H., 2013. Does temperature or runoff control the feedback between chemical denudation and climate? Insights from NE Iceland. *Geochim. Cosmochim. Acta* 107, 65–81.
- Etheridge, M.A., 1983. Differential stress magnitudes during regional deformation and metamorphism: upper bound imposed by tensile fracturing. *Geology* 11, 231–234.
- Felmy, A.R., Qafoku, O., Arey, B.W., Hu, J.Z., Hu, M., Schaefer, T.H., Ilton, E.S., Hess, N.J., Pearce, C.I., Feng, J., Rosso, K.M., 2012. Reaction of water-saturated supercritical CO₂ with forsterite: evidence for magnesite formation at low temperatures. *Geochim. Cosmochim. Acta* 91, 271–282.
- Fredlund, D., Rahardjo, H., 1993. *Soil Mechanics for Unsaturated Soils*. John Wiley & Sons, Inc., New York.
- Fricker, K.J., Park, A.-H.A., 2013. Effect of H₂O on Mg(OH)₂ carbonation pathways for combined CO₂ capture and storage. *Chem. Eng. Sci.* 100, 332–341.
- Gautier, J.-M., Oelkers, E.H., Schott, J., 2001. Are quartz dissolution rates proportional to B.E.T. surface areas? *Geochim. Cosmochim. Acta* 65, 1059–1070.
- Gautier, Q., Bénézet, P., Mavromatis, V., Schott, J., 2014. Hydromagnesite solubility product and growth kinetics in aqueous solution from 25 to 75 °C. *Geochim. Cosmochim. Acta* 138, 1–20.
- Gherardi, F., Xu, T., Pruess, K., 2007. Numerical modeling of self-limiting and self-enhancing caprock alteration induced by CO₂ storage in a depleted gas reservoir. *Chem. Geol.* 244, 103–129.
- Gislason, S.R., Wolff-Boenisch, D., Stefansson, A., Oelkers, E.H., Gunnlaugsson, E., Sigurdardottir, H., Sigfusson, B., Broecker, W.S., Matter, J.M., Stute, M., 2010. Mineral sequestration of carbon dioxide in basalt: a pre-injection overview of the CarbFix project. *Int. J. Greenh. Gas Control* 4, 537–545.
- Gualtieri, A.F., 2000. Accuracy of XRPD QPA using the combined Rietveld ± RIR method research papers. *J. Appl. Crystallogr.* 33, 267–278.
- Hänchen, M., Prigiobbe, V., Baciocchi, R., Mazzotti, M., 2008. Precipitation in the Mg-carbonate system—effects of temperature and CO₂ pressure. *Chem. Eng. Sci.* 63, 1012–1028.
- Harrison, A.L., 2014. *Mechanisms of Carbon Mineralization from the Pore to Field Scale: Implications for CO₂ Sequestration* (Ph.D. Thesis) The University of British Columbia, Vancouver, Canada.
- Harrison, A.L., Power, I.M., Dipple, G.M., 2013a. Accelerated carbonation of brucite in mine tailings for carbon sequestration. *Environ. Sci. Technol.* 47, 126–134.
- Harrison, A.L., Power, I.M., Dipple, G.M., 2013b. Strategies for enhancing carbon sequestration in Mg-rich mine tailings. In: Brown, A., Figueroa, L., Wolkersdorfer, C. (Eds.), *Reliable Mine Technology vol. 1*. Publication Printers, Denver, Colorado, USA, pp. 593–598.
- Harrison, A.L., Dipple, G.M., Power, I.M., Ulrich Mayer, K., 2015. Influence of surface passivation and water content on mineral reactions in unsaturated porous media: implications for brucite carbonation and CO₂ sequestration. *Geochim. Cosmochim. Acta* 148, 477–495.
- Helgeson, H.C., Murphy, W.M., Aagaard, P., 1984. Thermodynamic and kinetic constraints on reaction rates among minerals and aqueous solutions. II. Rate constants, effective surface area, and the hydrolysis of feldspar. *Geochim. Cosmochim. Acta* 48, 2405–2432.
- Hill, S., 1952. Channelling in packed columns. *Chem. Eng. Sci.* 1, 247–253.
- Hodson, M.E., 2006. Searching for the perfect surface area normalizing term—a comparison of BET surface area-, geometric surface area- and mass-normalized dissolution rates of anorthite and biotite. *J. Geochem. Explor.* 88, 288–291.
- Hopkinson, L., Kristova, P., Rutt, K., Cressey, G., 2012. Phase transitions in the system MgO–CO₂–H₂O during CO₂ degassing of Mg-bearing solutions. *Geochim. Cosmochim. Acta* 76, 1–13.
- Hövelmann, J., Austrheim, H., Jamtveit, B., 2012a. Microstructure and porosity evolution during experimental carbonation of a natural peridotite. *Chem. Geol.* 334, 254–265.
- Hövelmann, J., Putnis, C.V., Ruiz-Agudo, E., Austrheim, H., 2012b. Direct nanoscale observations of CO₂ sequestration during brucite [Mg(OH)₂] dissolution. *Environ. Sci. Technol.* 46, 5253–5260.
- Jeen, S.-W., Mayer, K.U., Gillham, R.W., Blowes, D.W., 2007. Reactive transport modeling of trichloroethene treatment with declining reactivity of iron. *Environ. Sci. Technol.* 41, 1432–1438.
- Ji, W., Amine, D., Ahlfeld, D.P., Lin, J.D., Hill, E.I., 1993. Laboratory study of air sparging: air flow visualization. *Ground Water Monit. Remediat.* 13, 115–126.
- Johnson, N.C., Thomas, B., Maher, K., Rosenbauer, R.J., Bird, D., Brown, G.E., 2014. Olivine dissolution and carbonation under conditions relevant for in situ carbon storage. *Chem. Geol.* 373, 93–105.
- Kalia, N., Balakotaiah, V., 2007. Modeling and analysis of wormhole formation in reactive dissolution of carbonate rocks. *Chem. Eng. Sci.* 62, 919–928.
- Kampman, N., Bickle, M., Wigley, M., Dubacq, B., 2014. Fluid flow and CO₂–fluid–mineral interactions during CO₂–storage in sedimentary basins. *Chem. Geol.* 369, 22–50.
- Kelemen, P.B., Matter, J., 2008. In situ carbonation of peridotite for CO₂ storage. *Proc. Natl. Acad. Sci. U. S. A.* 105, 17295–17300.
- Kelemen, P.B., Whitehead, J.A., Aharonov, E., Jordahl, K.A., 1995. Experiments on flow focusing in soluble porous media, with applications to melt extraction from the mantle. *J. Geophys. Res.* 100, 475–496.
- Kelemen, P.B., Matter, J., Streit, E.E., Rudge, J.F., Curry, W.B., Blusztajn, J., 2011. Rates and mechanisms of mineral carbonation in peridotite: natural processes and recipes for enhanced, in situ CO₂ capture and storage. *Annu. Rev. Earth Planet. Sci.* 39, 545–576.
- King, H.E., Plümper, O., Putnis, A., 2010. Effect of secondary phase formation on the carbonation of olivine. *Environ. Sci. Technol.* 44, 6503–6509.
- Königsberger, E., Königsberger, L.-C., Gamsjäger, H., 1999. Low-temperature thermodynamic model for the system Na₂CO₃–MgCO₃–CaCO₃–H₂O. *Geochim. Cosmochim. Acta* 63, 3105–3119.
- Kristova, P., Hopkinson, L.J., Rutt, K.J., Hunter, H.M.A., Cressey, G., 2014. Carbonate mineral paragenesis and reaction kinetics in the system MgO–CaO–CO₂–H₂O in presence of chloride or nitrate ions at near surface ambient temperatures. *Appl. Geochem.* 50, 16–24.
- Kueper, B.H., Frind, E.O., 1988. An overview of immiscible fingering in porous media. *J. Contam. Hydrol.* 2, 95–110.
- Lackner, K.S., Wendt, C.H., Butt, D.P., Joyce, E.L., Sharp, D.H., 1995. Carbon dioxide disposal in carbonate minerals. *Energy* 20, 1153–1170.
- Lee, M.R., Hodson, M.E., Parsons, I., 1998. The role of intragranular microtextures and microstructures in chemical and mechanical weathering: direct comparisons of experimentally and naturally weathered alkali feldspars. *Geochim. Cosmochim. Acta* 62, 2771–2788.
- Levenspiel, O., 1999. *Chemical Reaction Engineering*. John Wiley & Sons, Inc.
- Li, T., Keener, T.C., Cheng, L., 2014. Carbon dioxide removal by using Mg(OH)₂ in a bubble column: effects of various operating parameters. *Int. J. Greenh. Gas Control* 31, 67–76.
- Lichtner, P.C., 1996. Continuum formulation of multicomponent–multiphase reactive transport. *Rev. Mineral. Geochem.* 34, 1–79.
- Loring, J.S., Thompson, C.J., Wang, Z., Joly, A.G., Sklarew, D.S., Schaefer, H.T., Ilton, E.S., Rosso, K.M., Felmy, A.R., 2011. In situ infrared spectroscopic study of forsterite carbonation in wet supercritical CO₂. *Environ. Sci. Technol.* 45, 6204–6210.
- Luquot, L., Gouze, P., 2009. Experimental determination of porosity and permeability changes induced by injection of CO₂ into carbonate rocks. *Chem. Geol.* 265, 148–159.
- Maher, K., 2011. The role of fluid residence time and topographic scales in determining chemical fluxes from landscapes. *Earth Planet. Sci. Lett.* 312, 48–58.
- Maher, K., Steefel, C.I., DePaolo, D.J., Viani, B.E., 2006. The mineral dissolution rate conundrum: insights from reactive transport modeling of U isotopes and pore fluid chemistry in marine sediments. *Geochim. Cosmochim. Acta* 70, 337–363.
- Maher, K., Steefel, C.I., White, A.F., Stonestrom, D.A., 2009. The role of reaction affinity and secondary minerals in regulating chemical weathering rates at the Santa Cruz Soil Chronosequence, California. *Geochim. Cosmochim. Acta* 73, 2804–2831.
- Manning, D.A.C., 2008. Biological enhancement of soil carbonate precipitation: passive removal of atmospheric CO₂. *Mineral. Mag.* 72, 639–649.
- Marulanda, C., Culligan, P.J., Germaine, J.T., 2000. Centrifuge modeling of air sparging — a study of air flow through saturated porous media. *J. Hazard. Mater.* 72, 179–215.
- Mason, E.A., Malinauskas, A.P., 1983. *Gas Transport in Porous Media: The Dusty-gas Model*. Elsevier, New York.
- Matter, J.M., Kelemen, P.B., 2009. Permanent storage of carbon dioxide in geological reservoirs by mineral carbonation. *Nat. Geosci.* 2, 837–841.
- Mayer, K.U., Frind, E.O., Blowes, D.W., 2002. Multicomponent reactive transport modeling in variably saturated porous media using a generalized formulation for kinetically controlled reactions. *Water Resour. Res.* 38, 1174.
- McGrail, B.P., Schaefer, H.T., Ho, A.M., Chien, Y.-J., Dooley, J.J., Davidson, C.L., 2006. Potential for carbon dioxide sequestration in flood basalts. *J. Geophys. Res.* 111, B12201.
- McKinley, J.P., Zachara, J.M., Liu, C., Heald, S.C., Prenzler, B.I., Kempshall, B.W., 2006. Microscale controls on the fate of contaminant uranium in the vadose zone, Hanford Site, Washington. *Geochim. Cosmochim. Acta* 70, 1873–1887.
- Miller, Q.R.S., Thompson, C.J., Loring, J.S., Windisch, C.F., Bowden, M.E., Hoyt, D.W., Hu, J.Z., Arey, B.W., Rosso, K.M., Schaefer, H.T., 2013. Insights into silicate carbonation processes in water-bearing supercritical CO₂ fluids. *Int. J. Greenh. Gas Control* 15, 104–118.
- Molins, S., Mayer, K.U., 2007. Coupling between geochemical reactions and multicomponent gas and solute transport in unsaturated media: a reactive transport modeling study. *Water Resour. Res.* 43, W05435.
- Mook, W., Bommerson, J., Staverman, W., 1974. Carbon isotope fractionation between dissolved bicarbonate and gaseous carbon dioxide. *Earth Planet. Sci. Lett.* 22, 169–176.
- Morgan, B., Wilson, S.A., Madsen, I.C., Gozukara, Y.M., Habsuda, J., 2015. Increased thermal stability of nesquehonite (MgCO₃·3H₂O) in the presence of humidity and CO₂: implications for low-temperature CO₂ storage. *Int. J. Greenh. Gas Control* 39, 366–376.
- National Instruments, 2008. *National Instruments (2008) LabVIEW V.8.6*. National Instruments, USA.
- Nduagu, E., Romão, I., Fagerlund, J., Zevenhoven, R., 2013. Performance assessment of producing Mg(OH)₂ for CO₂ mineral sequestration. *Appl. Energy* 106, 116–126.
- Ortoleva, P., Chadam, J., Merino, E., Sen, A., 1987. Geochemical self-organization II: the reactive-infiltration instability. *Am. J. Sci.* 287, 1008–1040.
- Pačes, T., 1983. Rate constants of dissolution derived from the measurements of mass balance in hydrological catchments. *Geochim. Cosmochim. Acta* 47, 1855–1863.
- Parkhurst, D.L., Appelo, C.A.J., 2013. Description of input and examples for PHREEQC version 3—A computer program for speciation, batch-reaction, one-dimensional transport, and inverse geochemical calculations: U.S. Geological Survey Techniques and Methods, book 6, chap. A43, p. 497 available only at <http://pubs.usgs.gov/tm/06/a43>.

- Petrovich, R., 1981. Kinetics of dissolution of mechanically comminuted rock-forming oxides and silicates—I. Deformation and dissolution of quartz under laboratory conditions. *Geochim. Cosmochim. Acta* 45, 1665.
- Pettenati, M., Mercury, L., Azaroual, M., 2008. Capillary geochemistry in non-saturated zone of soils. Water content and geochemical signatures. *Appl. Geochem.* 23, 3799–3818.
- Peuble, S., Godard, M., Luquot, L., Andreani, M., Martinez, I., Gouze, P., 2015. CO₂ geological storage in olivine rich basaltic aquifers: new insights from reactive-percolation experiments. *Appl. Geochem.* 52, 174–190.
- Pham, V.T.H., Lu, P., Aagaard, P., Zhu, C., Hellevang, H., 2011. On the potential of CO₂–water–rock interactions for CO₂ storage using a modified kinetic model. *Int. J. Greenh. Gas Control* 5, 1002–1015.
- Pokrovsky, O., Schott, J., 2004. Experimental study of brucite dissolution and precipitation in aqueous solutions: surface speciation and chemical affinity control. *Geochim. Cosmochim. Acta* 68, 31–45.
- Pokrovsky, O.S., Schott, J., Castillo, A., 2005. Kinetics of brucite dissolution at 25 °C in the presence of organic and inorganic ligands and divalent metals. *Geochim. Cosmochim. Acta* 69, 905–918.
- Power, I.M., Wilson, S.A., Thom, J.M., Dipple, G.M., Southam, G., 2007. Biologically induced mineralization of dypingite by cyanobacteria from an alkaline wetland near Atlin, British Columbia, Canada. *Geochem. Trans.* 8, 13.
- Power, I.M., Harrison, A.L., Dipple, G.M., Southam, G., 2013a. Carbon sequestration via carbonic anhydrase facilitated magnesium carbonate precipitation. *Int. J. Greenh. Gas Control* 16, 145–155.
- Power, I.M., Harrison, A.L., Dipple, G.M., Wilson, S.A., Kelemen, P.B., Hitch, M., Southam, G., 2013b. Carbon mineralization: from natural analogues to engineered systems. *Rev. Mineral. Geochem.* 77, 305–360.
- Power, I.M., Wilson, S.A., Harrison, A.L., Dipple, G.M., Mccutcheon, J., Southam, G., Kenward, P.A., 2014. A depositional model for hydromagnesite–magnesite playas near atlin, British Columbia, Canada. *Sedimentology* 61, 1701–1733.
- Pronost, J., Beaudoin, G., Tremblay, J., Constantin, M., 2011. Carbon sequestration kinetic and storage capacity of ultramafic mining waste. *Environ. Sci. Technol.* 45, 9413–9420.
- Renforth, P., Manning, D.A.C., Lopez-Capel, E., 2009. Carbonate precipitation in artificial soils as a sink for atmospheric carbon dioxide. *Appl. Geochem.* 24, 1757–1764.
- Renforth, P., Washbourne, C.-L., Taylder, J., Manning, D.A.C., 2011. Silicate production and availability for mineral carbonation. *Environ. Sci. Technol.* 45, 2035–2041.
- Saldi, G.D., Schott, J., Pokrovsky, O.S., Gautier, Q., Oelkers, E.H., 2012. An experimental study of magnesite precipitation rates at neutral to alkaline conditions and 100–200 °C as a function of pH, aqueous solution composition and chemical affinity. *Geochim. Cosmochim. Acta* 83, 93–109.
- Schaefer, H.T., Windisch, C.F., McGrail, B.P., Martin, P.F., Rosso, K.M., 2011. Brucite [Mg(OH)₂] carbonation in wet supercritical CO₂: an in situ high pressure X-ray diffraction study. *Geochim. Cosmochim. Acta* 75, 7458–7471.
- Schaefer, H.T., McGrail, B.P., Loring, J.L., Bowden, M.E., Arey, B.W., Rosso, K.M., 2013. Forsterite [Mg₂SiO₄] carbonation in wet supercritical CO₂: an in situ high-pressure X-ray diffraction study. *Environ. Sci. Technol.* 47, 174–181.
- Scherer, G.W., 2004. Stress from crystallization of salt. *Cem. Concr. Res.* 34, 1613–1624.
- Schuling, R.D., de Boer, P.L., 2010. Coastal spreading of olivine to control atmospheric CO₂ concentrations: a critical analysis of viability. Comment: nature and laboratory models are different. *Int. J. Greenh. Gas Control* 4, 855–856.
- Scislowski, A., Zuddas, P., 2010. Estimation of reactive mineral surface area during water–rock interaction using fluid chemical data. *Geochim. Cosmochim. Acta* 74, 6996–7007.
- Šimůnek, J., Šejna, M., Saito, M., van Genuchten, M.T., 2013. The Hydrus-1D Software Package for Simulating the One-dimensional Movement of Water, Heat, and Multiple Solutes in Variably-saturated Media. Department of Environmental Sciences, University of California Riverside, Riverside, USA.
- Stockmann, G.J., Wolff-Boenisch, D., Gislason, S.R., Oelkers, E.H., 2011. Do carbonate precipitates affect dissolution kinetics? 1: basaltic glass. *Chem. Geol.* 284, 306–316.
- Stockmann, G.J., Wolff-Boenisch, D., Gislason, S.R., Oelkers, E.H., 2013. Do carbonate precipitates affect dissolution kinetics? 2. Diopside. *Chem. Geol.* 337–338, 56–66.
- Thompson, C.J., Loring, J.S., Rosso, K.M., Wang, Z., 2013. Comparative reactivity study of forsterite and antigorite in wet supercritical CO₂ by in situ infrared spectroscopy. *Int. J. Greenh. Gas Control* 18, 246–255.
- Veblen, D., Ferry, J.M., 1983. A TEM study of the biotite–chlorite reaction and comparison with petrologic observations. *Am. Mineral.* 68, 1160–1168.
- Washbourne, C.-L., Renforth, P., Manning, D.A.C., 2012. Investigating carbonate formation in urban soils as a method for capture and storage of atmospheric carbon. *Sci. Total Environ.* 431, 166–175.
- White, A.F., Brantley, S.L., 2003. The effect of time on the weathering of silicate minerals: why do weathering rates differ in the laboratory and field? *Chem. Geol.* 202, 479–506.
- Wilson, S.A., Bish, D.L., 2012. Stability of Mg-sulfate minerals in the presence of smectites: possible mineralogical controls on H₂O cycling and biomarker preservation on Mars. *Geochim. Cosmochim. Acta* 96, 120–133.
- Wilson, S.A., Raudsepp, M., Dipple, G.M., 2006. Verifying and quantifying carbon fixation in minerals from serpentine-rich mine tailings using the Rietveld method with X-ray powder diffraction data. *Am. Mineral.* 91, 1331–1341.
- Wilson, S.A., Dipple, G.M., Power, I.M., Thom, J.M., Anderson, R.G., Raudsepp, M., Gabites, J.E., Southam, G., 2009. Carbon dioxide fixation within mine wastes of ultramafic-hosted ore deposits: examples from the Clinton Creek and Cassiar chrysotile deposits, Canada. *Econ. Geol.* 104, 95–112.
- Wilson, S.A., Barker, S.L.L., Dipple, G.M., Atudorei, V., 2010. Isotopic disequilibrium during uptake of atmospheric CO₂ into mine process waters: implications for CO₂ sequestration. *Environ. Sci. Technol.* 44, 9522–9529.
- Wilson, S.A., Harrison, A.L., Dipple, G.M., Power, I.M., Barker, S.L.L., Mayer, K.U., Fallon, S.J., Raudsepp, M., Southam, G., 2014. Offsetting of CO₂ emissions by air capture in mine tailings at the Mount Keith Nickel Mine, Western Australia: rates, controls and prospects for carbon neutral mining. *Int. J. Greenh. Gas Control* 25, 121–140.
- Zhao, L., Sang, L., Chen, J., Ji, J., Teng, H.H., 2010. Aqueous carbonation of natural brucite: relevance to CO₂ sequestration. *Environ. Sci. Technol.* 44, 406–411.